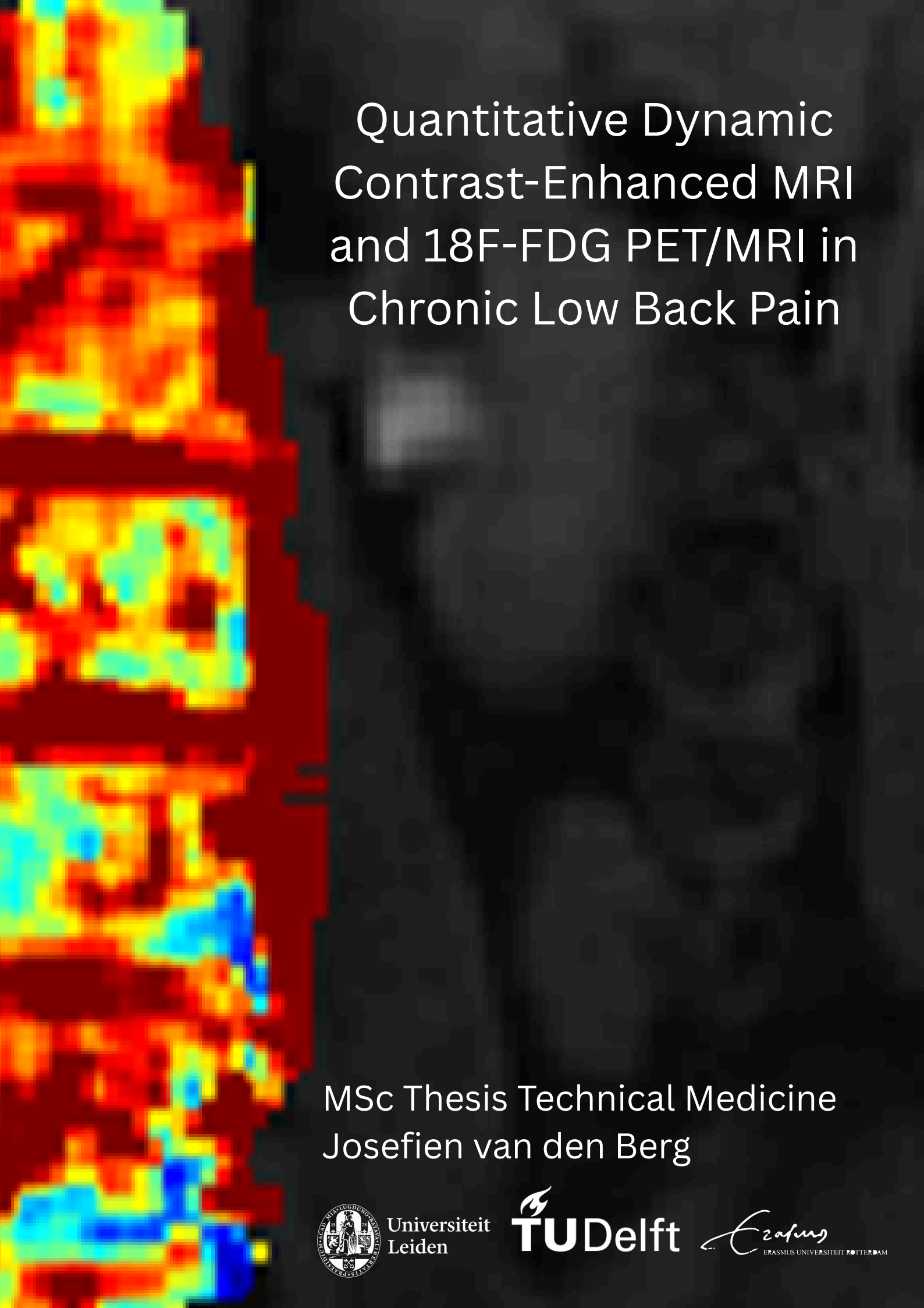

Quantitative Dynamic Contrast-Enhanced MRI and 18F-FDG PET/MRI in Chronic Low Back Pain

MSc Thesis Technical Medicine

Josefien van den Berg

Universiteit Leiden
TU Delft
Erasmus Universiteit Rotterdam

This page was left blank intentionally.

Quantitative Dynamic Contrast-Enhanced MRI and 18F-FDG PET/MRI in Chronic Low Back Pain

J.E. (Josefien) van den Berg
Student number: 4663381
10 Sep 2025

Thesis in partial fulfilment of the requirements for the joint degree of Master of Science in
Technical Medicine
Leiden University | Delft University of Technology | Erasmus University Rotterdam

Master thesis project (TM30004 | 35 ECTS)
Department of Radiology and Nuclear Medicine, Erasmus Medical Center
January 2025 – September 2025

Supervisors:
- Dr. R.A. (Rianne) van der Heijden
- Dr.ir. D.H.J. (Dirk) Poot
- J.M. (Marijn) Mostert

Thesis committee members:
- Dr. J.F. (Jifke) Veenland, TU Delft (chair)
- Dr. R.A. (Rianne) van der Heijden, Erasmus MC
- Dr.ir. D.H.J. (Dirk) Poot, Erasmus MC

Universiteit Leiden
TU Delft Delft University of Technology
Erasmus Universiteit Rotterdam

This page was left blank intentionally.

Summary

Chronic low back pain is a leading cause of disability worldwide, but most cases lack a pathoanatomical source on conventional imaging. The role of low-grade inflammation in chronic pain is increasingly understood. Hence, functional imaging techniques such as ^{18}F-Fluorodeoxyglucose positron emission tomography (^{18}F-FDG PET) and dynamic contrast-enhanced magnetic resonance imaging (DCE-MRI) may aid in the diagnosis of LBP by quantifying metabolic and microcirculatory aspects of inflammation, respectively. However, the relationship between these modalities in the lumbar spine remains unclear.

This thesis investigates the correlation between quantitative parameters of PET and DCE-MRI in the chronically painful lumbar spine. The secondary objective is to determine whether and how these correlations vary across different anatomical structures.

^{18}F-FDG PET/DCE-MRI images from 23 patients with chronic LBP were processed using an in-house developed software pipeline (SPARCK) with custom additions/modifications. Regions of interest (ROIs) were manually segmented in eight lumbar structures in areas of increased ^{18}F-FDG uptake and matched reference regions. PET parameters were SUV_{mean} and SUV_{max}. Pharmacokinetic modeling with the Extended Tofts model was applied to obtain median and peak K^{trans}, v_p and k_{ep} from DCE-MRI. Correlations were tested using rank-based linear mixed-effects model, accounting for repeated measures and skewed distributions. Significance levels were corrected for multiple testing.

Across the total of 179 ROIs, weak but significant positive correlations were observed between SUV and K^{trans} metrics ($\rho_{LME} \approx 0.31–0.37$), and between SUV and v_p metrics ($\rho_{LME} = 0.23$) except $SUV_{mean}/v_{p,peak}$. There were no significant correlations between SUV and k_{ep} metrics across all ROIs. Structure-specific analyses showed varying correlations between SUV and K^{trans} metrics: strong correlations in the intervertebral disc, moderate ρ_{LME} in the spinal canal and facet joint, no correlations in the nerve root and interspinous tissue.

Correlations between quantitative ^{18}F-FDG PET and DCE-MRI parameters in chronic LBP are weakly positive overall and vary across anatomical structures. These results suggest that the imaging modalities capture complementary rather than redundant aspects of inflammation and that their diagnostic value may depend on the anatomical structure under investigation. Future studies should validate these findings in larger cohorts and establish baseline parameter values with asymptomatic controls.

List of abbreviations

^{18}F-FDG	^{18}F-fluorodeoxyglucose
AIF	arterial input function
CA	contrast agent
DCE-MRI	dynamic contrast-enhanced magnetic resonance imaging
DISCO	differential subsampling with cartesian ordering
EES	extravascular and extracellular space
ETofts	extended Tofts model
i2w	image-to-world transform
IQR	interquartile range
LBP	low back pain
MRI	magnetic resonance imaging
PET	positron emission tomography
rmcorr	repeated measures correlation
ROI	region of interest
SD	standard deviation
SI	signal intensity
SPGR	spoiled gradient echo
SUV	standardized uptake value
TIC	time-intensity curve
T1w	T1-weighted magnetic resonance images

Contents

Introduction

Low back pain (LBP) is highly prevalent and a leading cause of disability worldwide, contributing substantially to healthcare utilization and economic burden (1). It was estimated that up to 10% of those affected with LBP will develop chronic LBP, lasting over three months (2). Imaging is not routinely recommended for chronic LBP, as conventional imaging (X-rays and computed tomography) does not improve clinical outcomes, while exposing patients to radiation (3). On magnetic resonance images (MRI), structural abnormalities do not correlate with symptoms, as similar findings are common in asymptomatic individuals (4–6). In fact, over 90% of LBP is non-specific, lacking a pathoanatomical cause (3,7). Without an identified pain source, therapies lack a treatment target and are often inadequate, with the risk of unnecessary surgeries and overuse of opioids as a result (6,8). As anatomic imaging often fails to pinpoint pain generators, a different approach is needed.

In recent years, it has been shown that chronic pain is correlated with low-grade inflammation. For example, immune mediators have been found in the serum and cerebrospinal fluid of patients with neuropathic pain (9,10). Impinged or damaged nerves are common causes of pain and are also thought to trigger a neuroinflammatory response (11). The role of inflammation is increasingly understood in the pathophysiology of age-related degeneration (12,13) and osteoarthritis (14). In patients with chronic low back pain and no clear anatomical lesion, inflammatory processes may underlie symptoms and remain undetected by conventional imaging. The presence of this inflammation can be a target of functional imaging in pain patients.

Functional imaging

Positron emission tomography

A well-known imaging technique to uncover inflammation is positron emission tomography (PET). PET is a quantitative imaging method that measures tissue function by detecting activity from an administered radiotracer. ^{18}F-Fluorodeoxyglucose (^{18}F-FDG) is a radioactive glucose analog that accumulates in tissues with high glucose metabolism. In inflamed tissues, metabolic activity is increased primarily due to activated inflammatory cells, which require glucose for their energy production (15). PET radiotracer activity is often quantified by calculating the standardized uptake value (SUV), which represents the tissue activity concentration corrected for the natural decay of an injected dose and normalized to the patient's weight.

PET in the spine

^{18}F-FDG PET has proven to be a useful modality in painful musculoskeletal diseases (5,16,17)[†]. In clinical practice, functional information from PET in hybrid ^{18}F-FDG PET/MRI helped reveal previously unidentified pain generators, leading to changes in patient management (18–21). Nerves in the lateral recess that were impinged due to a herniated disc showed higher values of SUV_{max} (maximum SUV) than the contralateral side (4). In addition to the inflammatory response, nociceptive signaling in the spinal cord involves increased neuronal activity, which depends on glucose metabolism. (22). Zhou et al. (22) reported higher ^{18}F-FDG uptake in the spinal canal of patients with low back pain compared to asymptomatic subjects.

[†] See also the literature review in Appendix C: Evaluating Inflammation in the Spine with ^{18}F-FDG PET and Contrast-Enhanced MRI, written in preparation of this thesis.

Dynamic contrast-enhanced MRI

To meet the increased metabolic demand, chronically inflamed tissues undergo microcirculatory changes. For example, tissues tend to form new vessels (neoangiogenesis) to increase blood supply (23). Regions with a rich blood supply can be visualized using contrast-enhanced MRI. However, static contrast-enhanced MRI (post-contrast imaging) provides only qualitative information of perfusion and is not able to quantify the speed of enhancement. Dynamic contrast-enhanced (DCE-) MRI allows quantification of different elements of microcirculation by repeatedly measuring contrast agent concentration over time. Some DCE parameters are directly related to (patho)physiological properties of tissue microvasculature (24,25). The following sections provide a technical overview of DCE-MRI.

Time-intensity curve

The principle of DCE or perfusion imaging is to monitor the passage of an intravenously injected paramagnetic contrast agent (CA) as it propagates through a tissue by repeated MRI acquisition. DCE-MRI relies on T1-weighted images. Gadolinium-based contrast agents reduce tissue T1 relaxation time, thereby increasing signal intensity (SI) on T1-weighted images. The resulting time-intensity curve (TIC) captures signal changes over time following contrast injection (Fig. 1). Because SI varies as a function of local CA concentration, the TIC provides a basis for quantifying tissue microcirculation, including perfusion, vascular permeability, and interstitial distribution (24,26).

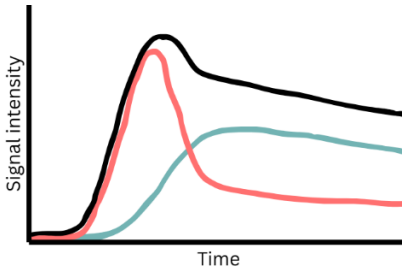

Figure 1. Schematic representation of a time-intensity curve. The total (black) is the sum of enhancement from contrast agent in the vascular system (arterial input and recirculation, red) and in the interstitium (dark cyan) (26).

In healthy tissue, the TIC typically follows a three-phase pattern. After intravenous contrast administration, the CA enters the capillaries and diffuses into the interstitial space due to a concentration gradient between plasma and interstitium. This wash-in phase is influenced by both tissue blood flow and vascular permeability. In well-perfused tissues, such as muscle or synovium, contrast arrives and equilibrates rapidly, whereas in less vascularized tissues, including ligaments or cartilage, the signal may rise more slowly or not at all. Following wash-in, contrast equilibrates between the vascular and interstitial space. Finally, SI decreases as contrast is cleared via venous and lymphatic drainage (26,27).

In the context of inflammation, a faster wash-in and elevated peak intensity are expected due to increased perfusion and vascular permeability (23). An elongated wash-out phase may follow due to prolonged retention of the CA, caused by immature, leaky neovessels and expanded interstitial space (23,28).

Quantitative analysis

Enhancement patterns can be analyzed in multiple ways. Qualitative or visual analysis focuses on the shape of the curve or digital subtraction images displaying contrast enhancement. Descriptive parameters, e.g. maximum enhancement, can be extracted in a semi-quantitative analysis, with or without so-called heuristic models. These parameters are useful, but lack a direct physiological correlate (29). This thesis focuses on quantitative analysis of the DCE-MRI signal. The benefit of quantitative parameters is that they are directly or more closely related to tissue physiology.

Furthermore, these parameters are theoretically independent of the scan protocol and patient biology, thereby improving inter- and intra-patient comparability (26).

The dynamic contrast-enhanced signal *A(t)* in each voxel is described by

$$A(t) = S_\xi\left(\left(AIF_\chi * P_\varphi\right)\right)(t)$$

where * represents convolution, and *S*, *AIF* and *P* are separate models with parameters ξ (ksi), χ (chi), and φ (phi), respectively (30). The arterial input function (AIF) describes how the contrast agent enters the feeding artery of the tissue. Since the measured time-intensity curve is a combination of tissue properties and this AIF (Fig. 1), the AIF is required to compute the residual function. This function represents the contrast agent in the tissue at a given time after a hypothetical instantaneous injection. The residual function is used to extract quantitative tissue properties. The pharmacokinetic model P is essentially a mathematical equation with a set of parameters ϕ describing tissue microvascular physiology, enabling the estimation of quantitative parameters from the measured signal. Different models vary in the number of free parameters they include, with simpler models favoring robustness and more complex models aiming for physiological detail (24). MR signal intensities are converted to contrast concentrations through model S. The combined model A is fitted to the observed TIC.

Parameters

The most commonly used model P in practice is the Tofts model, described as

$$C(t) = K^{trans}\, e^{-tk_{ep}} * C_a(t)$$

where *C(t)* and $C_a(t)$ are concentration-time curves in the tissue and feeding artery, respectively, and K^{trans} and k_{ep} are the parameters ϕ (31,32). The transfer constant K^{trans} describes the rate at which a contrast agent leaks from the vascular space to the extravascular extracellular space (EES) [min^{-1}]. It is a combination of perfusion and vascular permeability, depending on vascular status (33). K^{trans} is expected to increase in the presence of inflammation (24). The rate constant k_{ep} describes the leakage from the EES back into the vascular space [min^{-1}] (24). k_{ep} itself is not directly related to tissue physiology (33). It is defined as $k_{ep} = K^{trans} / v_e$, where v_e is a physiological metric describing the EES volume per unit volume of tissue [fraction] (24).

The standard Tofts model assumes a negligible amount of CA in the intravascular space, which is invalid in many, and especially well-vascularized tissues (32). To address this limitation, the Extended Tofts (ETofts) model adds v_p, which describes the fractional blood plasma volume [fraction] (31):

$$C(t) = v_p C_a(t) + K^{trans}\, e^{-tk_{ep}} * C_a(t)$$

v_p tends to increase with vasodilation and neoangiogenesis. The DCE parameters in ETofts are listed in Table 1 and schematically visualized in Figure 2.

Table 1. DCE-MRI parameters

Symbol	Parameter	Unit
K^{trans}	Transfer constant between blood plasma and EES	min^{-1}
v_e	Relative volume of EES in a volume of tissue	fraction
k_{ep}*	Rate constant between EES and blood plasma	min^{-1}
v_p	Relative volume of blood plasma in a volume of tissue	fraction

* $k_{ep} = K^{trans} / v_e$; *DCE-MRI: dynamic contrast-enhanced magnetic resonance imaging; EES: extravascular extracellular space*

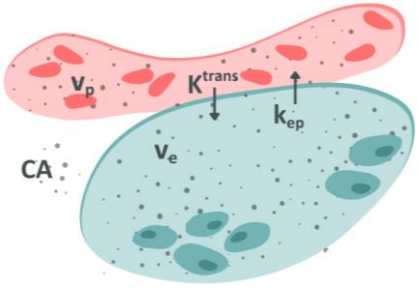

Figure 2. Visual representation of quantitative parameters in dynamic contrast-enhanced magnetic resonance imaging. *CA: contrast agent*

DCE-MRI in the spine

The number of DCE-MRI studies in the non-oncological spine is limited (34–38). Two studies found a positive correlation between intervertebral disc degeneration and perfusion of the lumbar vertebral marrow (36) and vertebral endplate (38). None of the studies reported quantitative parameters, such as K^{trans}. Hence, it remains unclear how quantitative DCE-MRI could aid in the diagnosis of chronic non-specific low back pain.

To recapitulate, ^{18}F-FDG PET detects inflammation by measuring increased glucose metabolism, whereas DCE-MRI can uncover inflammation by quantifying changes in microcirculation. Both functional imaging modalities could, in principle, identify inflammatory processes underlying chronic LBP, but their relationship remains unclear. If PET/MRI and DCE-MRI provide complementary information, their combined use could offer a more comprehensive assessment of LBP. On the other hand, if they yield similar information, one modality might suffice, and physicians could choose the most suitable option.

Currently, ^{18}F-FDG PET is the more established clinical tool for imaging inflammation. The clinical implementation of DCE-MRI has been confined mostly to the oncological domain (39–42). Each technique carries trade-offs: PET offers high sensitivity for metabolic changes, but involves ionizing radiation, high costs, and relatively low spatial resolution. Choosing DCE-MRI would allow the use of just one imaging method (MRI), but this technique is technically challenging, due to sensitivity to model parameters (e.g. AIF), noise and motion artifacts (26,32,43). Furthermore, the intravenous administration of contrast agents is generally well-tolerated, but holds risks related to allergic reaction, kidney failure and long-term gadolinium retention (44).

Understanding whether these modalities offer distinct or redundant information could help optimize imaging strategies for chronic LBP patients. Furthermore, the hypothesis is that PET/DCE correlations may differ depending on tissue-specific physiology and vascularization, so the imaging method may be tailored to the clinical indication.

Objectives

This study aims to investigate the correlation between quantitative PET and DCE-MRI parameters in patients with chronic low back pain. The secondary objective is to determine whether and how these correlations vary across different anatomical structures of the lumbar spine.

Methods

Patients

Imaging data were retrieved from a subset of the AMPHiBI trial data (19). This dataset includes patients aged 18-75 years with chronic LBP (≥ 3 months, numeric pain rating scale ≥ 6). Included patients received at least three months of conservative treatment according to Dutch guidelines (45), without improvement of symptoms (see Appendix A for all in- and exclusion criteria in the AMPHiBI trial). The current study included AMPHiBI patients who underwent baseline PET/MR imaging between May 2022 and March 2025. All images were visually checked for image quality. Patients were excluded in case of technical failure during acquisition or extensive artifacts. Inability to follow anatomic boundaries in a scan was also a reason for exclusion.

Image acquisition

Patients underwent whole-body PET/MR imaging with dedicated spine and (dynamic) contrast-enhanced sequences. Imaging was performed on a clinical 3T PET-MRI system (SIGNA PET/MR, GE Healthcare, Waukesha, WI, USA). Sequences relevant to this study are described below.

PET

Patients were required to fast for at least six hours before PET imaging. Acquisition started 55-70 minutes after the injection of 0.033 MBq/kg^2 ^{18}F-FDG (Fig. 3a). The whole body was imaged in 8-10 bed positions, with 3 minutes per bed position. Images were reconstructed using a Bayesian penalized likelihood algorithm (i.e. block-sequential regularized expectation maximization) with a β (beta) penalization factor of 450 (46). The field of view was 600x600x120 mm per bed position, with a pixel spacing of 2.34x2.34 mm and a slice thickness of 2.78 mm. MR-based attenuation correction was used in PET post-processing.

MRI

Simultaneously with PET imaging, whole-body T1-weighted images (T1w, Fig. 3b) were acquired at each bed position using a fast spoiled gradient echo (SPGR) pulse sequence and two-point Dixon image reconstruction for fat-water separation. The following acquisitions were performed in the lumbar spine and pelvis: Axial DESS (Double Echo Steady State) images were acquired for anatomical evaluation (Fig. 3c). Next, pre-contrast DISCO (DIfferential Subsampling with Cartesian Ordering) imaging was performed with a fast SPGR readout at flip angles 2° and 6° and two-point Dixon for subsequent T1 mapping (47). DISCO uses a three-dimensional SPGR with variable density pseudo-random k-space segmentation for increased acquisition speed (48). Both pre-contrast acquisitions were imaged with 6 frames at an interval of 2.8 seconds. B1 mapping was obtained using a gradient echo pulse sequence and Bloch-Siegert frequency shift (49). Dynamic contrast enhancement was measured using a DISCO imaging sequence at a 12° flip angle, hereafter referred to as the DCE image (Fig. 3d). DCE was acquired following an injection of 0.1 mL/kg body weight Gadolinium-based contrast agent (Gadovist, Bayer, Leverkusen, Germany) at 1.0 mL/s administration rate and a 15 mL saline flush. To capture early enhancement, 20 wash-in phases were recorded with a high temporal resolution of 2.7 seconds per phase. The following 35 phases were taken with a 12.9 second interval, leading to a total of 55 frames in 8m:22s. MRI pulse sequence details are provided in Table 2.

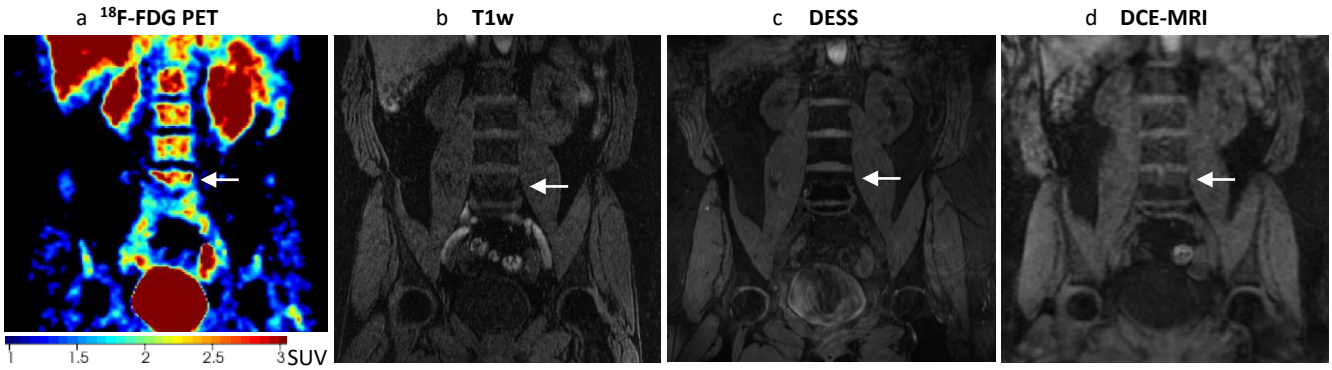

Figure 3. Coronal slices of images included in the PET/MRI acquisition protocol. The arrow indicates lumbar vertebra L5. a) *^{18}F-FDG PET: ^{18}F-Fluorodeoxyglucose positron emission tomography;* b) *T1w: T1-weighted fast spoiled gradient echo sequence*, water image; c) *DESS: double-echo steady-state;* d) *DCE-MRI: dynamic contrast-enhanced magnetic resonance imaging*, water image

Table 2. Magnetic resonance imaging acquisition parameters

Purpose	Sequence	TR [ms]	TE [ms]	FA [°]	Acquisition matrix	FOV [mm]	Image matrix	Slice thickness [mm]	NEX
Anatomical evaluation	FSPGR	5.1	1.8	15	356x356x120*	420x420x240*	512x512	2.0	1.0
Anatomical evaluation	DESS	21.0	6.7 / 35.3	30	512x512x250	500x500x500	512x512	2.0	1.0
B1 mapping	Gradient Echo	23.0	11.8	10	64x64x18	500x500x180	64x64	10.0	1.0
DCE imaging	DISCO	3.6	1.7	2 / 6 / 12	164x164x64**	500x500x192**	256x256	3.0	0.7

* Per bed position, 8-10 bed positions were acquired in PET/MR imaging. ** Number of slices was 60-66 in dynamic imaging. *TR: repetition time; TE: echo time; FA: flip angle; FOV: field-of-view; NEX: number of excitations; FSPGR: fast spoiled gradient echo; DESS: double-echo steady-state; DISCO: differential subsampling with Cartesian ordering; DCE: dynamic contrast-enhanced*

Image evaluation

PET/MR images were examined by a team of at least one nuclear medicine physician and one musculoskeletal radiologist, who reported imaging findings for clinical use and research purposes. The reports focused on identifying possible pain generators, based on PET findings, anatomical MRI and post-contrast MRI, but excluding DCE information. Their findings were considered as ground truth.

Image processing

The images were processed and analyzed using in-house developed software (SPARCK, Fig. 4) in MATLAB (Version 8.6.0, R2015b (50)). The existing SPARCK pipeline was extended with image registration, PET post-processing, data extraction and statistical analysis. Segmentations were performed in ITK-SNAP (Version 2.4.0 (51)), an open-source software application used for medical image segmentation. Image processing for each patient is described below. Successful completion of each step was verified by visual inspection.

Motion correction

The DISCO sequences were motion corrected by means of a Rigid groupwise registration method using the Elastix toolkit (Version 5.0.1 (52)). The groupwise method ensures equal weights of each image in the time series, to account for varying contrast intensity ranges due to the passing contrast bolus.

Fitvolume

The motion-corrected DCE series was exported to ITK-SNAP. Here, a fitvolume was segmented, which contained the lumbar spine, paravertebral muscles and sacroiliac joints, with a positive margin of approximately 1.5 cm. The fitvolume is used for T1-mapping and quantitative analysis.

T1-mapping

The first four frames of the DCE sequence were separated as the mask phase, where the contrast agent has not yet entered the imaging field of view. This mask was used, along with the two other DISCO sequences with flip angles 2° and 6° and the B1-map, to fit the T1 map in the fitvolume (53). The T1 map provides native T1 relaxation times in each voxel, i.e. before contrast enhancement.

Quantitative analysis

Arterial input function

The population-based AIF by Parker et al. was used to analyze the fitvolume (25). This model provides a high-temporal-resolution standardized AIF, improving the reproducibility of DCE-MRI modeling.

Pharmacokinetic modeling

The time-intensity curve for each voxel in the fitvolume was analyzed with the Extended Tofts model to obtain quantitative parameters K^{trans}, k_{ep}, and v_p (31).

Conversion of signal intensity to contrast concentration

Signal intensities were modeled using a standard SPGR signal equation, with one free parameter $\xi = S_0$. S_0 is the pre-contrast signal intensity estimated from the T1 map. The model was then inverted to obtain T1 relaxation times, which were further converted into contrast agent concentration C(t) using the known relaxivity of the CA (30). Maximum likelihood estimation was used to determine model parameters ξ, χ, and ϕ with the constraints provided in Table 3.

Table 3. Parameters, units and constraints applied during pharmacokinetic modeling

Parameter	K^{trans} [min^{-1}]	k_{ep} [min^{-1}]	v_p [fraction]
Lower bound optimization	0	0	0
Lower bound initialization	0.01	0.01	0.001
Upper bound optimization	0.5	0.5	0.001
Upper bound initialization	1	2	0.2
Step size	0.0002	0.01	0.0001

SUV conversion

PET activity images were converted to SUV by the following equation implemented in SPARCK:

$$SUV = \frac{A_c / e^{-\lambda t}}{D_{injected}} * BW$$

where A_c is the activity concentration in [Bq/mL], $D_{injected}$ is the injected dose in [Bq], which should be corrected for natural decay at time t after injection and the decay factor $\lambda = \log 2 / T_{1/2}$. The time point used was at the start of the PET acquisition. The half-life $T_{1/2}$ of radioisotope ^{18}F is 109.77 minutes. The activity was normalized by multiplying by patient's body weight BW in grams.

Image registration

PET and DCE scans must be coregistered in order to compare parameters within the same regions. In general, medical image registration can be performed using rigid, affine, or nonlinear (deformable) transformations (54). In this study, rigid registration was chosen because all images were acquired in the same scanning session, minimizing large misalignments, and because the anatomical structures of interest are relatively rigid, reducing the need for more complex transformations. Rigid registration involves the modification of the image-to-world transform (i2w), which defines the mapping from image coordinates to world coordinates. The i2w is defined by:

- Origin: the world coordinates of the first voxel, often the upper-left voxel of the first slice;
- Orientation: two orthogonal direction cosines defining the rotation of rows and columns in world space;
- Spacing: voxel size in mm along each axis.

Since PET images were acquired simultaneously with T1w MR images, the superior spatial resolution and anatomic detail of T1w can be leveraged for registration. Typically, the initial spatial alignment between images is preserved via metadata stored in the image headers. In some patients, initial alignment was lost, possibly due to technician intervention during scanning. For these cases, a bony anatomical landmark was manually identified in both image sets. The translation between these points was calculated and applied to the i2w of the T1w and PET images.

Subsequently, all T1w images were rigidly registered to the DCE images using an Euler transform. In this step, the rigid body transformation was applied directly to the i2w transformation matrix, without resampling to preserve the original spatial resolution and fine anatomical detail of the MR images. The transformation was then applied to the SUV-converted PET image. This time, resampling was necessary to match the spatial resolution of DCE images, and B-Spline interpolation was used to preserve smoothness of the image (55). For anatomical guidance during segmentation, DESS images were also rigidly registered to DCE without resampling.

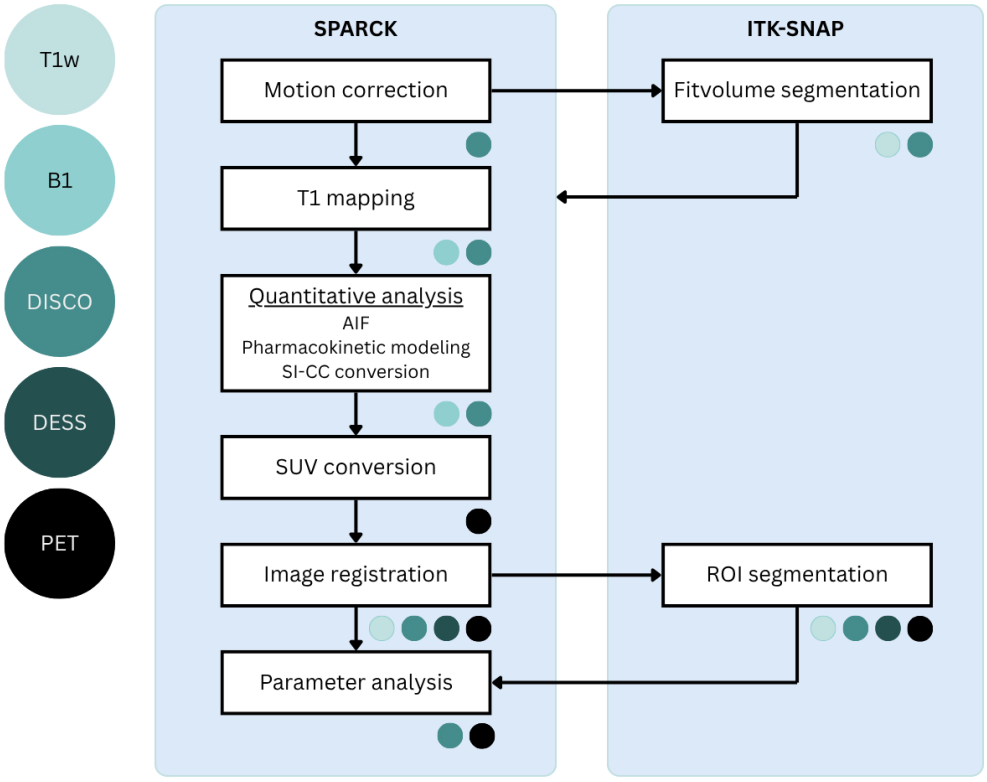

Figure 4. Schematic overview of the SPARCK pipeline. *T1w: T1-weighted magnetic resonance imaging (MRI); DISCO: DIfferential Subsampling with Cartesian Ordering; DESS: double-echo steady-state MRI; PET: positron emission tomography; DCE: dynamic contrast-enhanced MRI; AIF: arterial input function; SI: signal intensity; CC: contrast concentration; SUV: standardized uptake value; ROI: region of interest*

Image analysis

Regions of interest

Regions of interest (ROIs) were manually segmented by the first author in ITK-SNAP, following training by the reporting radiologist (RH). Segmentations were reviewed in consultation with RH to reduce observer-related errors.

In ITK-SNAP, the mask phase of the DCE series was used as base layer, ensuring equal spatial resolution of the segmentations and the parameter maps. The registered and resampled PET image was loaded as overlay and scaled to 1-3 SUV, corresponding to the settings of the reporting physicians. Registered T1w and DESS images were additionally loaded for anatomical reference. ROIs were confined within anatomical boundaries to analyze PET/DCE correlations for different structures of the spine. The following anatomical structures in spinal levels L1 through S1 were investigated: spinal canal, lateral recess, neuroforamen, extraforaminal nerve, facet joint space, perifacet region (containing synovium), intervertebral disc, and interspinous tissue.

Lesion selection was based on PET findings, as this is the reference standard modality. Areas of increased ^{18}F-FDG that were mentioned in the conclusion of the radiologic reports were segmented. Contrast-enhancement findings were not considered during segmentation to avoid biasing the PET/DCE correlation analysis. Reference ROIs were drawn in anatomical structures corresponding to segmented lesions, either contralaterally or at a different lumbar level. These regions were not segmented in a one-to-one ratio with lesions. Instead, an arbitrary number of reference ROIs was created to capture representative values from anatomically corresponding but PET-negative regions, thereby creating a wider distribution of parameter values for analysis.

Quantitative parameters

Parameters were extracted from ROIs using custom-developed additions to SPARCK. Preliminary data were visualized in histograms to inspect distributions. DCE parameters K^{trans}, k_{ep}, and v_p displayed right-skewed distributions, thus median values were extracted. In conventional DCE analyses, median values are typically derived from regions showing strong contrast enhancement (38,39,56–58). In this study, however, ROIs were defined by ^{18}F-FDG uptake, which may cover relatively large heterogeneous areas. This could artificially lower the DCE medians. However, maximum values in DCE are highly susceptible to noise, poor model fitting, and motion artifacts (26). To capture focal abnormalities more reliably, peak values (e.g. K^{trans}_{peak}) were calculated as the average of the maximum voxel and its surrounding 3x3x3 cube (approximately 1.0 mL volume as recommended by the European Association of Nuclear Medicine for PET imaging (59)). Voxels outside of the ROI were not included in the calculation.

For PET, standardized uptake values were normally distributed, therefore both mean and maximum SUV (SUV_{mean} and SUV_{max}) were extracted. Although SUV_{max} is also sensitive to noise, it remains the established clinical standard and was thus reported rather than SUV_{peak}.

Statistical analysis

All statistical analyses were also performed in SPARCK. Grouped PET parameters were reported as mean and standard deviation (SD), and DCE parameters as median and interquartile range (IQR) based on their respective distributions.

For improved statistical robustness, lesion and reference ROIs from several structures were combined based on anatomical coherence:

- Facet joint space and perifacet region were combined as ‘facet joint’;
- Lateral recess, neuroforamen, and extraforaminal nerve were grouped as ‘nerve root’.

Correlations between PET and DCE parameters were assessed by fitting a linear mixed-effects model (LME) (60), described as

$$y = X\beta + Zb + \varepsilon$$

where *y* is the response vector (e.g. K^{trans}_{median}), *X* is the fixed-effects matrix (e.g. SUV_{max}), and β is the model slope, reflecting the relationship between the response and fixed effects. The term *Zb* refers to the random effects matrix and *ε* describes the residual error, which includes noise. In our analysis, a random intercept per patient was included to account for subject-level variation. DCE parameters were strongly skewed, so all variables were rank-transformed, yielding a nonparametric Spearman-style correlation. The fitted slopes (ρ_{LME} = β) reflect the direction and strength of rank-based correlations, corrected for repeated measures.

In an additional analysis, correlations were explored using repeated measures correlation (rmcorr) on ranked data (61). Rmcorr is similar to the Pearson correlation, but adjusted for within-subject variability by subtracting the subject mean from each data point (analysis of covariance). The correlation coefficient ρ_{rm} ranges between -1 and 1:

$$\rho_{rm} = \frac{\sum X_c Y_c}{\sqrt{\sum X_c^2 \sum Y_c^2}}$$

where X_c and Y_c are within-subject centered ranks.

Correlations were explored across all ROIs combined and within each anatomical structure. For each structure, twelve models were fit to test associations between rank-transformed mean and maximum SUV, and median and peak K^{trans}, k_{ep}, and v_e. The significance threshold α = 0.05 was Bonferroni-corrected to 0.0042 for multiple comparisons. Scatter plots of raw (non-ranked) K^{trans}_{median} and SUV_{max} were shown, as these are clinically the most common parameters. Linear trend lines in scatter plots are shown for visualization purposes only and were not used for statistical inference.

Results

Data selection

Figure 5 shows the data selection schematically. Baseline PET/MR images of 38 patients were collected from the AMPHiBI trial dataset. Five patients were excluded because of technical failure: two patients had DISCO sequences with complete fat/water swaps, and their water images were missing; one patient was excluded due to failed DCE acquisition; one patient was excluded due to multiple fat/water swaps across the lumbar spine in multiple phases of the dynamic series which could compromise pharmacokinetic fitting; and one patient was excluded because motion correction in SPARCK was failed due to inconsistent image-to-world transform metadata of the DCE series had. The remaining 33 scans were processed with ETofts.

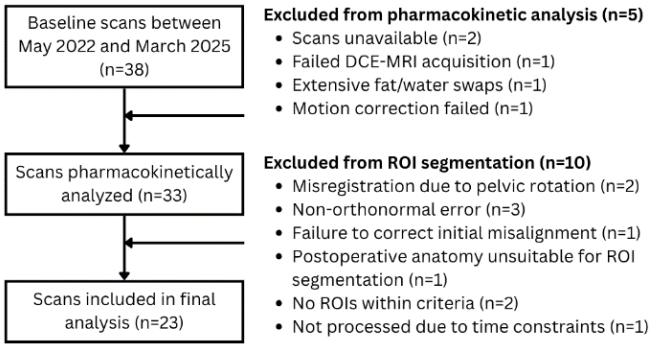

Figure 5. Data selection pipeline. *DCE-MRI: dynamic contrast-enhanced magnetic resonance imaging; ROI: region of interest*

In further analysis, six scans were excluded because PET/DCE registration failed: in two cases due to rotation of the pelvis, preventing accurate rigid registration; three images could not be loaded into ITK-SNAP due to non-orthonormal direction coefficients[‡]; in one case, the PET image failed to align while correcting initial misalignment. In one patient, anatomical bounds could not be maintained due to extensive deformations following surgery. One scan was not processed due to time constraints. Finally, 23 scans were included for ROI segmentation and parameter extraction. Among included patients, 15 (65%) were female, mean age was 49.5 years (SD 13.4) and average body mass index was 26.66 (SD 3.94). Maximum perceived pain score was on average 7.87 (SD 1.26) as reported on the numeric rating scale.

[‡] An orthonormal direction matrix contains vectors which are perpendicular to each other (orthogonal) and each vector has a length of one (normalized).

Regions of interest

Segmentation characteristics regarding numbers and size are provided in Table 4. The sizes were reported as median (IQR) based on their right-skewed distribution. Briefly, 179 ROIs were obtained, of which 104 lesions and 75 reference regions. On average, there were 4.5 (range 1–12) lesions and 3.2 (range 1–6) references per patient. Most ROIs were located in the perifacet region (N=51), followed by the facet joint space (N=28) and the intervertebral disc (N=26). Median size of all ROIs was 331.87 mm^3 (IQR 400.35). ROIs in structures of the nerve root (median 68.66–97.27 mm^3) were generally smaller than in other structures (median 343.31–446.31 mm^3).

Table 4. Number (lesions / references) and size (median (interquartile range)) of regions of interest.

	Number	**Size** [mm^3]
Total	179 (104 / 75)	331.87 (400.53)
Spinal canal	12 (8 / 4)	343.31 (703.79)
Lateral recess	14 (7 / 7)	68.66 (34.33)
Neuroforamen	17 (9 / 8)	91.55 (54.36)
Extraforaminal nerve	10 (5 / 5)	97.27 (57.22)
Facet joint space	28 (14 / 14)	440.59 (331.87)
Perifacet region	51 (31 / 20)	446.31 (452.03)
Intervertebral disc	26 (15 / 11)	400.53 (286.09)
Interspinous tissue	21 (15 / 6)	389.09 (317.57)

Parameter values

PET and DCE parameters for lesions and references in all ROIs and per anatomical structure are provided in Table 5. Generally, SUV, K^{trans}, and v_p values tended to be lower in the reference regions compared to lesions, while k_{ep} appeared higher in reference ROIs. One anomaly was the nerve root, where median and peak K^{trans} values tended to be higher in the reference regions than the lesions.

Among structures, the interspinous tissues appeared to have the highest SUV_{max} in both lesions (2.77 ± 0.55) and reference regions (1.47 ± 0.26). In lesions, K^{trans}_{median} tended to be highest in the facet joints (lesions 0.080 min^{-1} (0.054)). Reference ROIs across the facet joint and nerve root displayed similar values of K^{trans}_{median} (0.054 min^{-1} (IQR 0.033 and 0.056, respectively)). $v_{p,median}$ which seemed the highest in the nerve root lesions (0.021 (0.015)) and facet joint references (0.014 (0.006)). Finally, $k_{ep,median}$ appeared the highest in lesions and references of the intervertebral disc (0.230 min^{-1} (0.233) and 0.544 min^{-1} (0.914), respectively).

Table 5. PET (mean ± SD) and DCE-MRI (median (IQR)) parameters.

		SUV		K^{trans} [min^{-1}]		v_p [fraction]		k_{ep} [min^{-1}]	
	ROI type	Mean	Max	Median	Peak	Median	Peak	Median	Peak
All	Lesion (N=104)	1.84 ± 0.37	2.38 ± 0.68	0.057 (0.055)	0.096 (0.165)	0.014 (0.013)	0.023 (0.020)	0.141 (0.201)	0.341 (0.401)
	Reference (N=75)	1.06 ± 0.23	1.34 ± 0.26	0.040 (0.050)	0.076 (0.104)	0.012 (0.009)	0.019 (0.018)	0.167 (0.238)	0.445 (0.621)
Structures									
Spinal canal	Lesion (N=8)	1.71 ± 0.14	2.09 ± 0.34	0.020 (0.094)	0.053 (0.236)	0.008 (0.006)	0.012 (0.014)	0.218 (0.256)	0.410 (0.376)
	Reference (N=4)	1.11 ± 0.22	1.39 ± 0.20	0.006 (0.003)	0.007 (0.014)	0.004 (0.003)	0.007 (0.004)	0.063 (0.110)	0.248 (0.584)
Nerve root	Lesion (N=21)	1.68 ± 0.27	1.94 ± 0.33	0.043 (0.045)	0.054 (0.059)	0.021 (0.015)	0.022 (0.017)	0.141 (0.121)	0.204 (0.196)
	Reference (N=20)	1.22 ± 0.17	1.38 ± 0.23	0.054 (0.056)	0.071 (0.075)	0.011 (0.008)	0.015 (0.009)	0.160 (0.206)	0.295 (0.269)
Facet joint	Lesion (N=45)	1.77 ± 0.33	2.40 ± 0.64	0.079 (0.054)	0.169 (0.200)	0.018 (0.010)	0.026 (0.023)	0.165 (0.208)	0.456 (0.553)
	Reference (N=34)	1.01 ± 0.21	1.34 ± 0.25	0.054 (0.032)	0.124 (0.119)	0.015 (0.006)	0.029 (0.016)	0.183 (0.200)	0.637 (0.543)
Intervertebral disc	Lesion (N=15)	1.98 ± 0.49	2.72 ± 0.99	0.046 (0.055)	0.066 (0.146)	0.011 (0.009)	0.016 (0.020)	0.230 (0.233)	0.390 (0.271)
	Reference (N=11)	0.84 ± 0.19	1.22 ± 0.35	0.006 (0.008)	0.014 (0.006)	0.009 (0.005)	0.010 (0.005)	0.544 (0.914)	1.029 (1.023)
Interspinous tissue	Lesion (N=15)	2.20 ± 0.32	2.77 ± 0.55	0.053 (0.029)	0.094 (0.077)	0.007 (0.009)	0.014 (0.020)	0.056 (0.077)	0.162 (0.351)
	Reference (N=6)	1.18 ± 0.17	1.47 ± 0.26	0.039 (0.033)	0.050 (0.051)	0.007 (0.007)	0.016 (0.009)	0.090 (0.154)	0.229 (0.430)

PET: positron emission tomography; SD: standard deviation; DCE: dynamic contrast-enhanced magnetic resonance imaging; IQR: interquartile range; SUV: standardized uptake value; ROI: region of interest

Correlation between DCE-MRI and PET parameters

The LME-based correlation matrix of ranked data across all ROIs, and the distribution of raw (non-ranked) values of SUV_{max} and K^{trans}_{median} are shown in Figure 6. We observed moderate significant correlations between metrics of K^{trans} and SUV, which was strongest for K^{trans}_{median} and SUV_{mean} (ρ_{LME} = 0.37, p = 0.000). There were also weak but significant correlations between v_p metrics and SUV metrics. The correlation between $v_{p,peak}$ and SUV_{mean} was not significant after Bonferroni correction. The observed negative correlation between $k_{ep,peak}$ and SUV_{mean} (ρ_{LME} = -0.18, p = 0.0140) was no longer significant after correction.

In the spinal canal (Fig. 7), K^{trans}_{peak} was strongly correlated with SUV_{max} (ρ_{LME} = 0.80, p = 0.0009). Before Bonferroni, there were also significant correlations between K^{trans}_{peak} / SUV_{mean} (ρ_{LME} = 0.73, p = 0.0043), and K^{trans}_{median} / SUV_{max} (ρ_{LME} = 0.52, p = 0.0494). $v_{p,peak}$ and $k_{ep,median}$ showed moderate-to-strong positive correlations with SUV metrics before correction. Loss of significance may be due to low statistical power in this group, with just 12 data points across four patients.

In the nerve root (Fig. 8), $v_{p,median}$ showed a coefficient of ρ_{LME} = 0.30 with both SUV_{mean} and SUV_{max}. These correlations were not significant after Bonferroni correction (p = 0.0477 and 0.0439, respectively). All other DCE parameters showed no correlations with SUV metrics.

All K^{trans} and SUV metrics were weakly correlated in the facet joint (Fig. 9). The strongest correlation was between K^{trans}_{median} and SUV_{mean} (ρ_{LME} = 0.36, p = 0.0005). The weak correlations between K^{trans}_{peak} and SUV metrics were not significant after Bonferroni correction. $v_{p,median}$ was weakly correlated with SUV metrics before Bonferroni correction, while $v_{p,peak}$ showed no correlation to SUV metrics. There were no significant correlations between k_{ep} metrics and SUV metrics.

In the intervertebral disc (Fig. 10), we observed strong correlations between K^{trans}_{median} / SUV_{mean}, and K^{trans}_{peak} and SUV metrics (ρ_{LME} = 0.75, p = 0.0000 for all), and a moderate correlation between K^{trans}_{median} and SUV_{max} (ρ_{LME} = 0.55, p = 0.0025). SUV metrics were also strongly correlated with $v_{p,peak}$ (ρ_{LME} = 0.63, $p \leq$ 0.0006). Median v_p was moderately correlated with SUV_{mean} before correction, but not with SUV_{max}. There were no significant correlations between k_{ep} metrics and SUV metrics.

K^{trans} and SUV metrics showed moderate correlations in the interspinous tissue (Fig. 11), which was strongest between K^{trans}_{peak} and SUV_{max} (ρ_{LME} = 0.52, p = 0.0111). These correlations were not significant after Bonferroni correction. There were no correlations between SUV and v_p or k_{ep}. With 21 data points across eight patients, this group may also be underpowered.

Results from the rmcorr analysis were added in Appendix B.

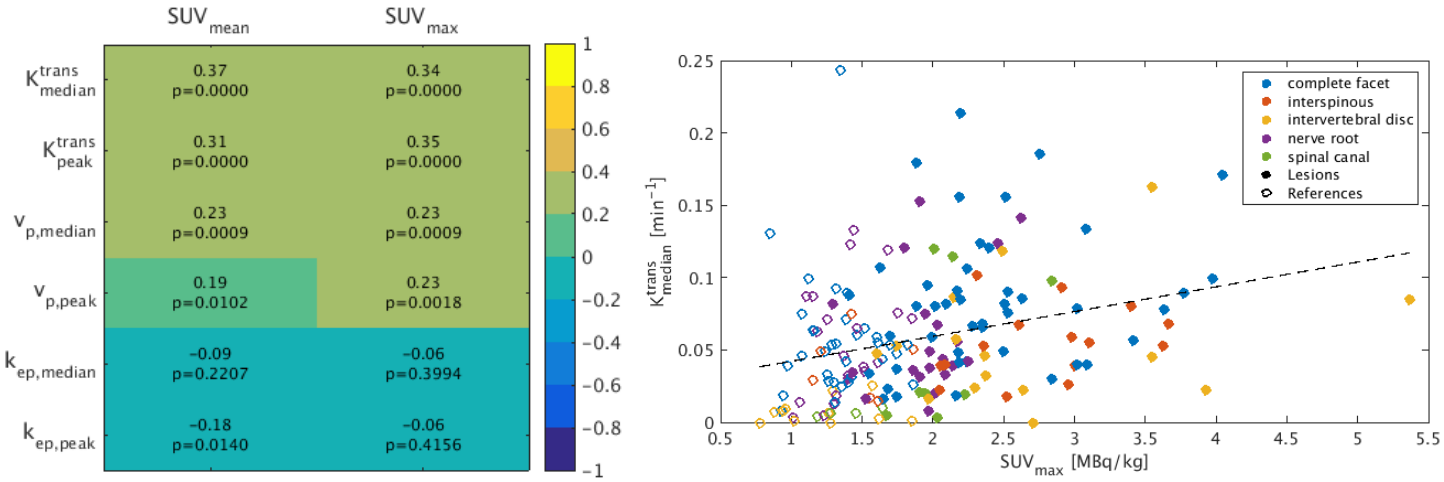

Figure 6. Results in all regions of interest combined. Left: Linear mixed-effects model coefficients on ranked data. Right: Scatter plot of original SUV_{max} and K^{trans}_{median}. Linear trend line is shown for visualization purposes only. *SUV: standardized uptake value*

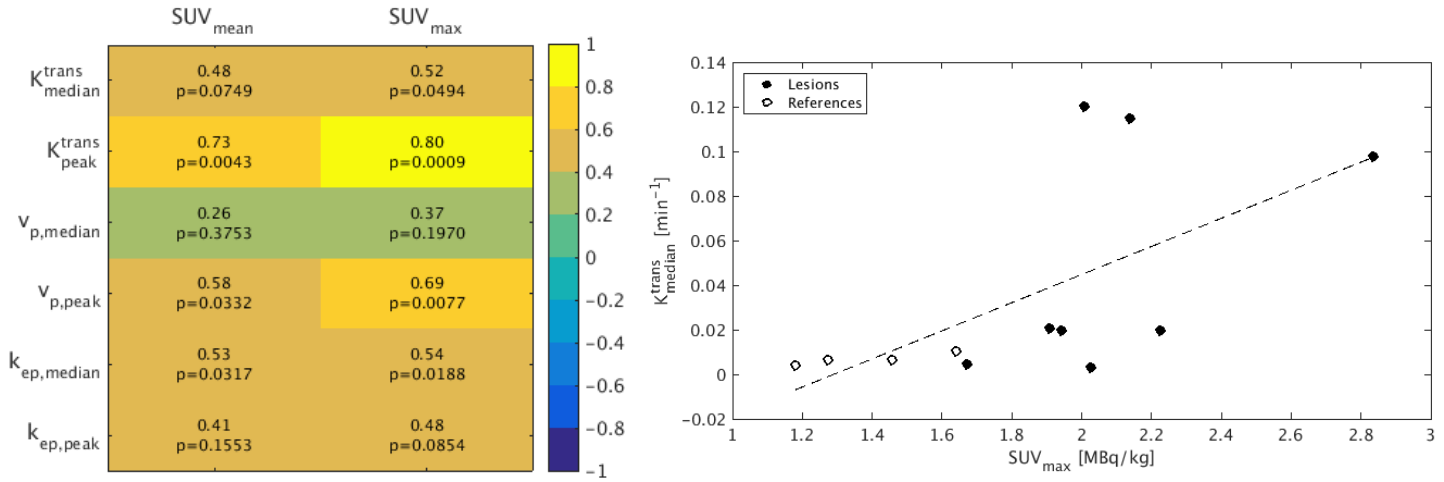

Figure 7. Results in the spinal canal. Left: Linear mixed-effects model coefficients on ranked data. Right: Scatter plot of original SUV_{max} and K^{trans}_{median}. Linear trend line is shown for visualization purposes only. *SUV: standardized uptake value*

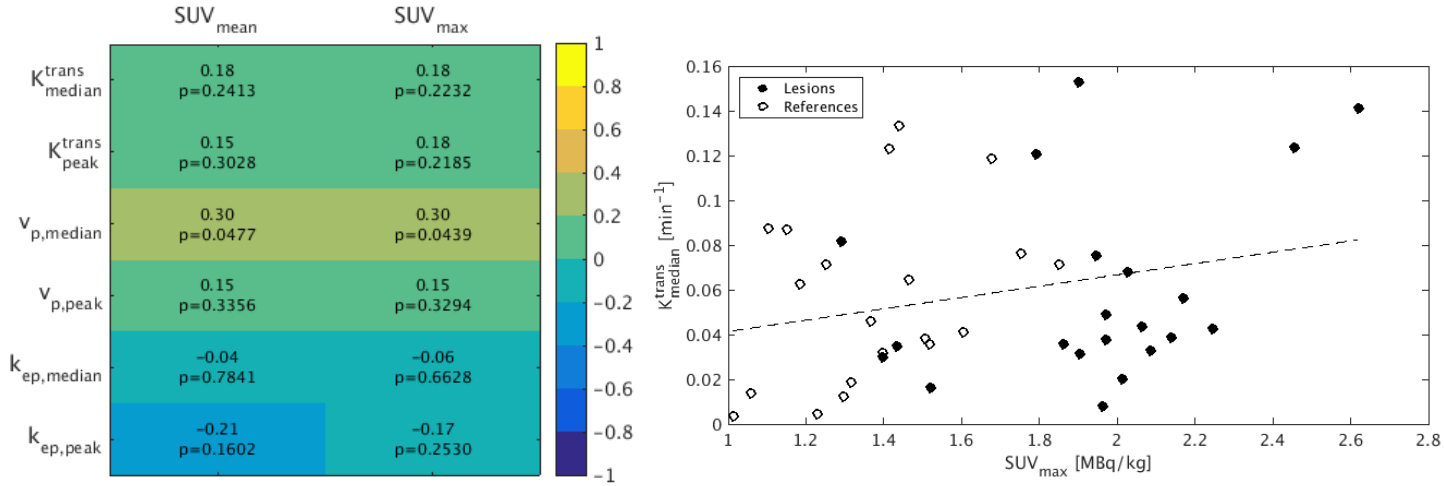

Figure 8. Results in the nerve root. Left: Linear mixed-effects model coefficients on ranked data. Right: Scatter plot of original SUV_{max} and K^{trans}_{median}. Linear trend line is shown for visualization purposes only. *SUV: standardized uptake value*

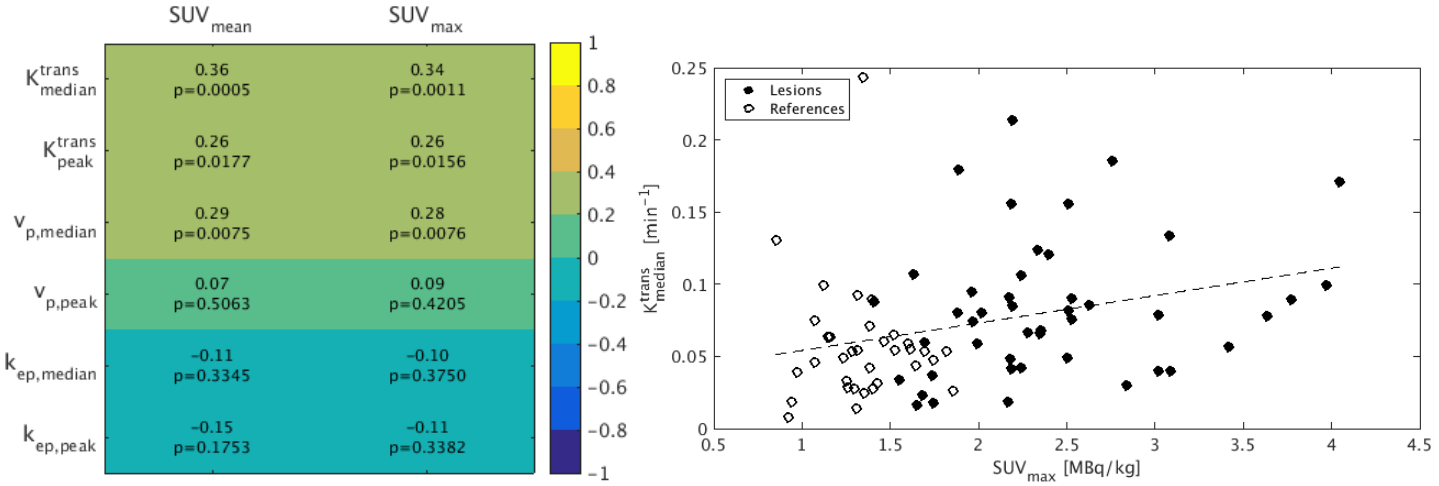

Figure 9. Results in the facet joint. Left: Linear mixed-effects model coefficients on ranked data. Right: Scatter plot of original SUV_{max} and K^{trans}_{median}. Linear trend line is shown for visualization purposes only. *SUV: standardized uptake value*

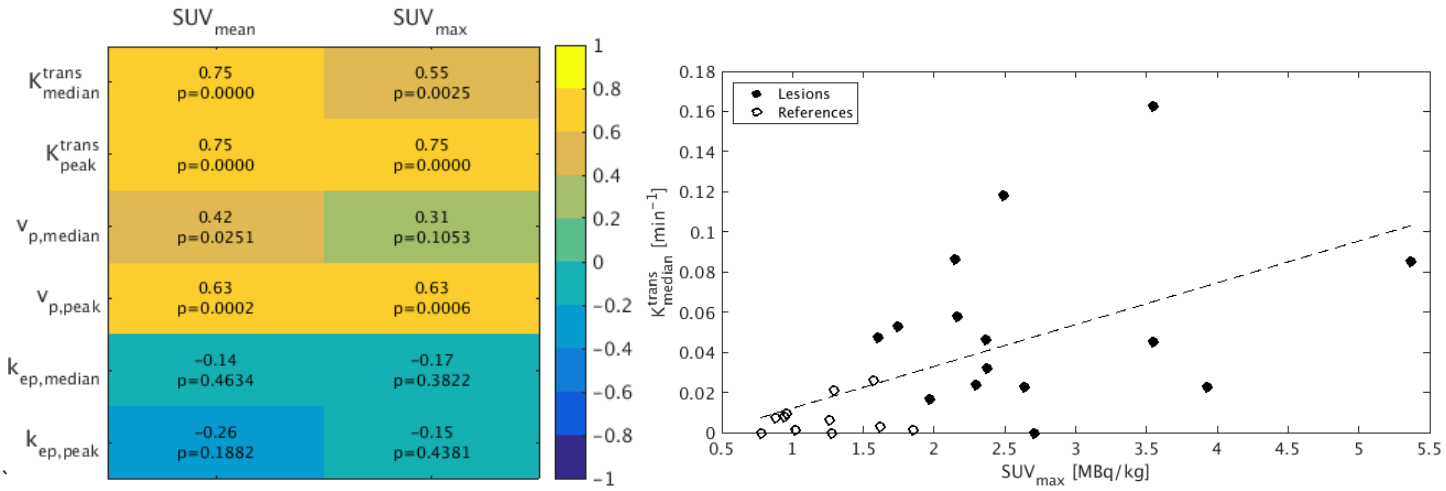

Figure 10. Results in the intervertebral disc. Left: Linear mixed-effects model coefficients on ranked data. Right: Scatter plot of original SUV_{max} and K^{trans}_{median}. Linear trend line is shown for visualization purposes only. *SUV: standardized uptake value*

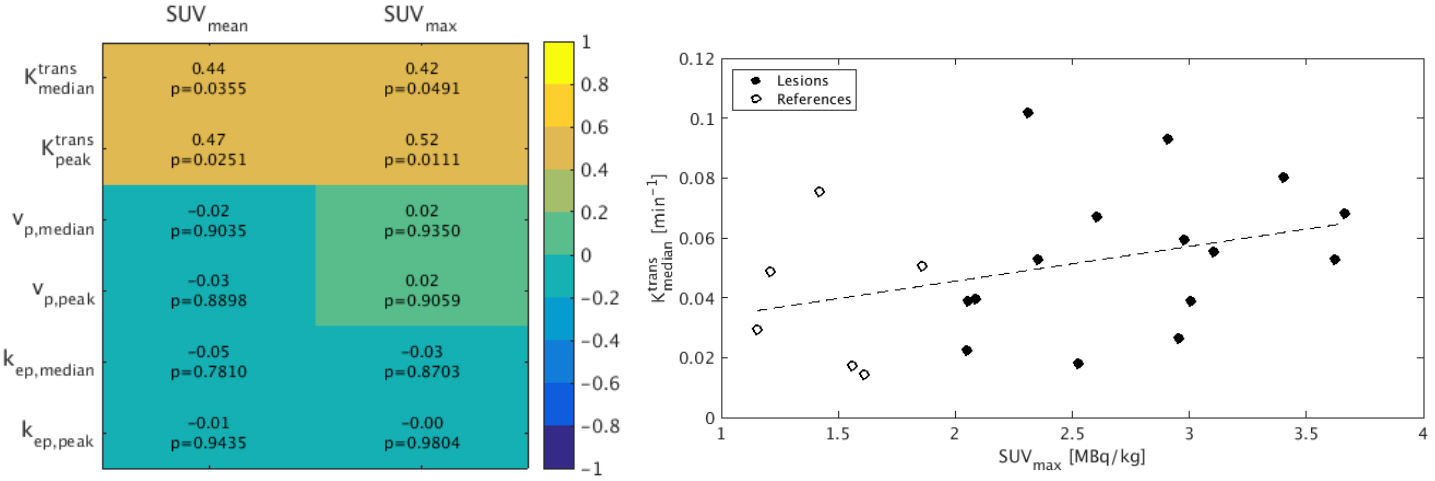

Figure 11. Results in the interspinous tissue. Left: Linear mixed-effects model coefficients on ranked data. Right: Scatter plot of original SUV_{max} and K^{trans}_{median}. Linear trend line is shown for visualization purposes only. *SUV: standardized uptake value*

Discussion

This is the first study to perform pharmacokinetic modeling of the entire lumbar spine and quantitatively evaluate the correlation between DCE-MRI and ^{18}F-FDG PET parameters. Understanding the correlation between quantitative markers of inflammation from the two imaging techniques may uncover more information about the pathophysiology of pain. Furthermore, this could help physicians choose the appropriate imaging modality to uncover the pain source in patients with chronic low back pain.

We observed weak positive correlations between all metrics of K^{trans} and SUV when analyzing all ROIs collectively. These findings suggest that areas in the lumbar spine with higher ^{18}F-FDG uptake may also exhibit increased perfusion and/or vascular permeability. This aligns with the understanding that both increased glucose metabolism and altered microcirculation are characteristic features of inflammatory processes (15,62). Although DCE-MRI and ^{18}F-FDG PET provide similar insights into inflammatory activity, the modest correlation strength implies that each modality may capture distinct underlying biological mechanisms. Consequently, these imaging techniques should currently not be viewed as interchangeable tools for identifying potential pain sources.

There were also weak correlations between SUV and v_p metrics in all ROIs, suggesting that higher ^{18}F-FDG uptake in a tissue corresponds with higher blood plasma volumes. After correcting for multiple comparisons, there were no significant correlations between k_{ep} and SUV metrics, suggesting there is no connection between the rate constant and ^{18}F-FDG uptake in the lumbar spine. However, issues with fitting and interpretation of v_p and k_{ep} are common in DCE-MRI. The parameter v_p is often considered unreliable due to low signal-to-noise ratio, especially in poorly vascularized tissues (32). Furthermore, stability of the estimation of k_{ep} requires scanning times of up to 15 minutes (63). Therefore, the results found with these parameters should be interpreted with caution.

Since microcirculatory traits vary across tissues (23,62), PET/DCE correlations were also investigated in anatomical structures separately. Positive correlations between SUV metrics and K^{trans} metrics seemed strong in the intervertebral disc, and moderate in the spinal canal and facet joints. In contrast, no significant correlations were observed in the nerve root and interspinous tissue. In the nerve root, all LME model slopes were low ($\rho_{LME} \leq 0.30$). This could indicate that PET and DCE may reflect distinct aspects of inflammation, or that ^{18}F-FDG uptake in nerve roots may be driven by metabolic processes unrelated to inflammation. Although the correlations in the interspinous tissue were also non-significant, the LME slopes were moderately high ($\rho_{LME} \approx 0.42–0.52$). This may indicate a true relationship that was underpowered for detection. Our findings support the idea that imaging markers of inflammation may correlate differently across specific spinal structures and the preferred imaging modality could be tailored to the suspected pain source, but larger studies are needed to confirm the observed correlations.

Few studies have evaluated quantitative parameters of DCE-MRI in the central and peripheral nervous system. Our findings of K^{trans}_{median} in the spinal canal and nerve root are in line with previously reported values of K^{trans} in the spinal cord of rats (64), and peripheral nerves in diabetic patients (65), respectively. The difference between $K^{trans}_{median}/SUV_{mean}$ and $K^{trans}_{peak}/SUV_{max}$ correlations in the spinal canal was notable. Upon inspection of the ROIs on DCE parameter maps, spillover of high values from adjacent vertebrae was observed, rendering peak and maximal metrics less reliable here. This effect

was previously described by Patel et al. (66), who suggest normalization against bone marrow uptake as a solution.

Lesions in all structure types tended to show higher K^{trans} values compared to the reference ROIs, except in the nerve root. K^{trans} in nerve root lesions tended to be lower compared to reference ROIs (K^{trans}_{median} 0.043 min^{-1} (0.045) vs. 0.054 min^{-1} (0.056)). Similarly, Jende et al. reported reduced K^{trans} in peripheral nerves of type II diabetic patients with diabetic neuropathy (DN) compared to those without DN (0.037 min^{-1} ± 0.010 vs. 0.046 min^{-1} ± 0.014) (65). Endothelial damage is thought to reduce vascular permeability, contributing to nerve ischemia and subsequent nerve injury. Damage to the endothelial cells lining blood vessels has also been associated with chronic inflammation (23,62,65,67). These findings raise the possibility that reduced perfusion, rather than increased permeability, may underlie pathophysiological changes associated with inflammation or pain in spinal nerve lesions.

To our knowledge, no perfusion studies of the facet joint exist. Other synovial joints, including the knee and wrist, may serve as a model. Median K^{trans} values across our facet joint lesions and references (0.079 and 0.054 min^{-1}) were higher than those reported in rheumatoid arthritis of the wrist (~ 0.010—0.040 min^{-1})(56), osteoarthritic knees (~ 0.035 min^{-1}) and healthy knees (~ 0.020 min^{-1})(57). This may be explained by differences in ROI segmentation. The studies mentioned only considered enhancing areas of the synovium. In our study, the boundaries of the articular processes were considered part of the 'facet joint' entity, therefore the joint segmentations included some bony tissue. Bones are known to be highly vascularized (68). Furthermore, vertebral bone and subchondral bone have shown short time to peak enhancement, suggesting high perfusion (69). Our findings of moderate associations between K^{trans} and SUV in the facet joint are in line with previously described co-localization of elevated ^{18}F-FDG uptake and high rate of early enhancement in inflamed synovia (56,70).

Nutrient supply to the disc occurs primarily via diffusion from the adjacent vertebral endplate rather than vascular perfusion (71). Therefore, previous DCE-MRI studies have investigated perfusion of the vertebral endplate and subchondral bone as indirect markers of disc physiology (38,72). Vascular ingrowth has been described in herniated discs (73), although this effect may be localized and not accountable for generalized correlations across the disc (74). We found strong correlations between metrics of SUV and both K^{trans} and v_p in the intervertebral disc. However, contamination from the vertebral bone was also observed. The results should be interpreted with caution and confirmed with larger studies.

Degeneration of the interspinous ligament has been associated with vascular invasion (75), but we found no correlations between v_p and SUV metrics in tissue. The observed moderate correlations between K^{trans} and SUV were not significant after correcting for multiple comparisons, but this may be the result of low statistical power, rather than underlying physiology. Unfortunately, we found no DCE-MRI studies of the interspinous tissue to corroborate our findings.

Direct quantitative correlations between DCE and PET parameters are seldom reported in literature, as most studies focus on diagnostic outcomes. To our knowledge, the only other paper that directly compared DCE and PET quantitative parameters in the spine is by Zhang et al. (39) in spinal tumors. Across malignant, borderline, and benign tumors, they found no significant correlations between SUV_{max} and both K^{trans} and k_{ep}. In a study of combined ^{18}F-FDG PET and DCE-MRI in atherosclerosis,

Truijman et al. (58) reported a weak but significant correlation between inflammation as measured by increased ^{18}F-FDG uptake and neoangiogenesis quantified by K^{trans}. The shared conclusion across these studies is in line with ours, suggesting that the lack of a strong correlation could indicate the complementary roles of DCE-MRI and PET.

Limitations

DCE-MRI

DCE-MRI presents inherent limitations related to both pharmacokinetic modeling and acquisition parameters. By considering v_p, the extended Tofts model is more accurate in highly perfused tissues than the standard Tofts model. On the other hand, ETofts may be more susceptible to fitting errors due to increased complexity (31,32). Since vascularization is expected to increase in inflamed tissue, ETofts was deemed the most appropriate choice for this study. However, in poorly vascularized regions such as the intervertebral disc and spinal canal, this model may introduce greater uncertainty (32). Findings must be interpreted with caution due to the potential unreliability of the model in these regions. In future studies, tailoring the pharmacokinetic model to the vascular characteristics of each tissue could improve accuracy but would increase processing time. By contrast, the current single-model approach of the entire fitvolume provides efficiency and allows post-hoc analyses across multiple structures.

Furthermore, the use of a literature-based population AIF may lead to systematic errors in parameter estimation. While a subject-specific AIF accounts for intersubject variability, it can also introduce noise and variability in parameter estimation (25). Given the diversity of tissue types analyzed in this exploratory study, the use of a standardized AIF was considered appropriate to enhance robustness and reproducibility across subjects.

Segmentation

Some uncertainty in ROI segmentation arose from both technical and methodological challenges. The spatial resolution of the dynamic images was impaired by a large field of view in dynamic sequences combined with high temporal resolution required to capture early enhancement (26). The voxel volume in DISCO sequences was approximately 11.44 mm^3, which introduces a significant partial volume effect. This complicated segmentation accuracy and may lead to inaccurate estimation of enhancement parameters, particularly in small structures.

Given the clinical context of chronic low back pain, it is not unexpected that patients may shift positions between scans to alleviate discomfort. For example, pelvic rotation was observed when a patient placed an arm beneath their right hip. Patient motion results in spatial misalignments between scans, for which rigid registration was employed. This method is robust, but it does not account for local deformations or more complex patient movements. Consequently, regional misalignments may persist, introducing uncertainty in the anatomical localization and accuracy of segmentations, especially in small structures like the nerve root. An affine registration would have been more appropriate, as it can compensate for translation, rotation, scaling, and shearing (76). However, affine transforms can produce images with non-orthonormal direction matrices, which are not supported by ITK-SNAP. For practical reasons, transitioning to a different segmentation platform was not feasible, and rigid registration was ultimately chosen as a compromise between robustness and practicality.

Future work should focus on enhancing segmentation reliability. Improving the image quality is a difficult task given the challenges that come with dynamic imaging. Reducing the field of view could improve spatial resolution while preserving temporal resolution, although smaller voxels may lead to a lower signal-to-noise ratio. Furthermore, deformable registration methods (and supporting segmentation software) or motion-reducing positioning aids during acquisition are recommended to minimize misalignments and improve segmentation reliability.

Peak metric

K^{trans} is typically reported as the median across a region because this is less sensitive to outlies and better represent non-normally distributed data. However, the median may obscure focal abnormalities of potential clinical relevance, especially in large or heterogeneous ROIs. For example, in Figure 12, a perifacet lesion demonstrated focally increased K^{trans} compared with diffusely increased SUV in the synovium.

To capture focal increases while avoiding noise sensitivity of maximal values, we reported 1 mL peak values. This peak metric also has limitations. Due to small and irregularly shaped ROIs, the theoretical voxel count for a peak mask (27) was not consistently met. In practice, the average number of voxels contributing to the peak value was only 8 (SD 3.7), which may reduce comparability across ROIs and limit interpretability. Furthermore, the peak metric is still susceptible to spillover from adjacent tissues. This effect was seen in the spinal canal and the intervertebral disc, and could have occurred in other structures. Using a negative marging during segmentation could reduce this error, but this would substantially reduce the ROI size.

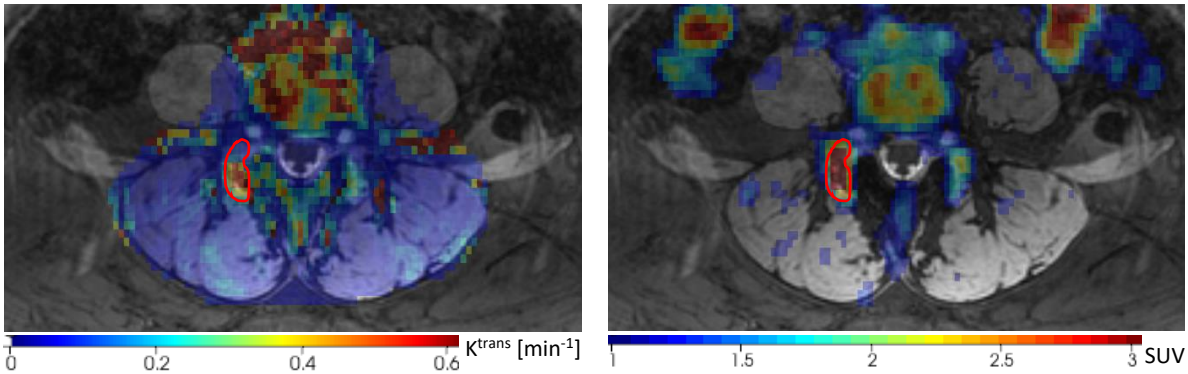

Figure 12. Example lesion ROI (red contour) in the right perifacet region at level L4/L5 showing focally increased K^{trans} (left) versus diffusely inreased SUV (right). Parameter maps are shown as overlay images on the DESS scan. *ROI: region of interest; SUV: standardized uptake value; DESS: double-echo steady-state*

Reporting both mean/median and peak/maximum values can provide insight into parameter distributions. Across all ROIs, the relative difference between K^{trans}_{median} and K^{trans}_{peak} was 71%, while the difference between SUV_{mean} and SUV_{max} was only 28%. This may reflect true focal increases in perfusion/permeability (K^{trans}), compared to diffuse increases in glucose metabolism, focal DCE peaks may also be the result of noise and model instability, as discussed previously. Another contributing factor may be differences in spatial resolution. PET images initially had a lower spatial resolution than DCE-MRI. Upsampling to a finer grid redistributes the PET signal across smaller voxels, potentially smoothing or diluting focal uptake and artificially reducing SUV_{max}. By contrast, the higher native resolution of DCE-MRI preserves local peaks, possibly exaggerating the relative difference between K^{trans} and SUV metrics.

Lesion selection

Lesion segmentation in this study was guided by radiological reports, focusing on regions of increased ^{18}F-FDG uptake. This approach was not only practical, given the detailed PET descriptions available, but also clinically meaningful, as it prioritized areas potentially responsible for the patient's symptoms. A limitation of this PET-guided approach might be the potential underdetection of pain sources that exhibit abnormal DCE parameters but normal ^{18}F-FDG uptake. Vascular changes may precede immune cell activation in early or low-grade inflammation (77), suggesting that DCE-MRI could potentially detect lesions missed by PET. Given the technical challenges of DCE-MRI and the focus on PET/DCE correlations, PET-guided segmentation was considered the most practical and clinically relevant strategy.

Statistical method

Finally, we would like to address the statistical method used in this work. To assess correlations while accounting for complexity of the data, ranked linear mixed-effects models were fitted. Ranking provides a Spearman-like approach for skewed data. The LME incorporates patient-specific intercepts to account for baseline differences, while estimating a fixed slope that reflects the direction and relative strength of the correlation. Unlike Spearman's ρ, this slope is not constrained between -1 and 1, which may limit its direct interpretability. Nevertheless, this general method provides insight into associations, and can be extended with multiple predictors and covariates if desired.

We briefly explored the rmcorr method, which produces a bounded correlation coefficient that may be easier to interpret. We observed similar results in terms of coefficients ρ_{rm} and ρ_{LME}, but significance levels varied notably; rmcorr generally produced higher p-values than LME. These differences were not explored extensively due to time limitations, and more extensive understanding of p-value computation in these methods is necessary. Future work should focus on finding the most suitable statistical method for this complex data, and consultation with a statistician is recommended.

Future recommendations

Future studies should include asymptomatic subjects to establish a baseline of normal PET and DCE characteristics. Such data are largely absent in the current literature, but are essential in distinguishing physiological from pathological patterns. Furthermore, comprehensive segmentation of all spinal structures would enable more detailed analysis of lesion distribution and tissue heterogeneity. We have suggested that the imaging method may be tailored to clinical indication. However, more research is needed to evaluate the predictive value of both modalities in identifying pain generating lesions. Approaches such as applying a Z-score threshold to parameter maps could allow for unbiased lesion identification. Cohen's Kappa could then quantify agreement between PET- and DCE-positive lesion maps, while ROC analysis could identify thresholds yielding optimal sensitivity and specificity for lesion detection. However, all of this relies on the robustness of quantitative DCE implementation.

Conclusion

We investigated the correlation between quantitative parameters of ^{18}F-FDG PET and DCE-MRI as markers of inflammation in the chronically painful lumbar spine. Overall, weak correlations were found between glucose metabolism and blood perfusion parameters. Per-structure analyses revealed strong correlation in intervertebral discs, moderate correlations in the spinal canal and facet joints, and no correlation in the nerve root and interspinous tissue. These results suggest that the imaging

methods capture complementary rather than redundant aspects of inflammation and that their diagnostic value may depend on the anatomical structure under investigation. Future studies should validate these findings in larger cohorts and establish baseline parameter values with asymptomatic controls.

References

1. Ferrari AJ, Santomauro DF, Aali A, Abate YH, Abbafati C, Abbastabar H, et al. Global incidence, prevalence, years lived with disability (YLDs), disability-adjusted life-years (DALYs), and healthy life expectancy (HALE) for 371 diseases and injuries in 204 countries and territories and 811 subnational locations, 1990–2021: a systematic analysis for the Global Burden of Disease Study 2021. The Lancet. 2024 May;403(10440):2133–61.
2. Meucci RD, Fassa AG, Faria NMX. Prevalence of chronic low back pain: systematic review. Rev Saúde Pública. 2015 Oct 5;49:1.
3. Hall AM, Aubrey-Bassler K, Thorne B, Maher CG. Do not routinely offer imaging for uncomplicated low back pain. The BMJ. 2021 Feb 12;372:n291.
4. Cipriano PW, Yoon D, Gandhi H, Holley D, Thakur D, Hargreaves BA, et al. ^{18} F-FDG PET/MRI in Chronic Sciatica: Early Results Revealing Spinal and Nonspinal Abnormalities. J Nucl Med. 2018 Jun;59(6):967–72.
5. Kogan F, Yoon D, Teeter MG, Chaudhari AJ, Hales L, Barbieri M, et al. Multimodal positron emission tomography (PET) imaging in non-oncologic musculoskeletal radiology. Skeletal Radiol [Internet]. 2024 Mar 16 [cited 2024 Apr 3]; Available from: https://link.springer.com/10.1007/s00256-024-04640-4
6. Lehman VT, Diehn FE, Broski SM, Nathan MA, Kemp BJ, Larson NB, et al. Comparison of [^{18} F] FDG-PET/MRI and Clinical Findings for Assessment of Suspected Lumbar Facet Joint Pain: A Prospective Study to Characterize Candidate Nonanatomic Imaging Biomarkers and Potential Impact on Management. Am J Neuroradiol. 2019 Sep 26;ajnr;ajnr.A6224v1.
7. Koes BW, van Tulder MW, Thomas S. Diagnosis and treatment of low back pain. BMJ. 2006 Jun 17;332(7555):1430–4.
8. Yoon D, Kogan F, Gold GE, Biswal S. Identifying Musculoskeletal Pain Generators Using Clinical PET. Semin Musculoskelet Radiol. 2020 Aug;24(4):441–50.
9. Bäckryd E, Lind AL, Thulin M, Larsson A, Gerdle B, Gordh T. High levels of cerebrospinal fluid chemokines point to the presence of neuroinflammation in peripheral neuropathic pain: a cross-sectional study of 2 cohorts of patients compared with healthy controls. Pain. 2017 Dec;158(12):2487–95.
10. Moen A, Lind AL, Thulin M, Kamali-Moghaddam M, Røe C, Gjerstad J, et al. Inflammatory Serum Protein Profiling of Patients with Lumbar Radicular Pain One Year after Disc Herniation. Int J Inflamm. 2016;2016:3874964.
11. Kogan F, Broski SM, Yoon D, Gold GE. Applications of PET-MRI in musculoskeletal disease: PET-MRI of MSK Disease. J Magn Reson Imaging. 2018 Jul;48(1):27–47.
12. Aliyev A, Saboury B, Kwee TC, Torigian DA, Basu S, Christensen HW, et al. Age-related inflammatory changes in the spine as demonstrated by 18F-FDG-PET: Observation and insight into degenerative spinal changes. Hell J Nucl Med. 2012;15(3):197-201+268.
13. Podichetty VK. The aging spine: the role of inflammatory mediators in intervertebral disc degeneration. Cell Mol Biol Noisy--Gd Fr. 2007 May 30;53(5):4–18.
14. Berenbaum F. Osteoarthritis as an inflammatory disease (osteoarthritis is not osteoarthrosis!). Osteoarthritis Cartilage. 2013 Jan;21(1):16–21.
15. Zhuang H, Alavi A. 18-Fluorodeoxyglucose positron emission tomographic imaging in the detection and monitoring of infection and inflammation. Semin Nucl Med. 2002 Jan 1;32(1):47–59.
16. Katal S, Clifford TG, Matcuk G, Eibschutz L, Gholamrezanezhad A. Clinical Applications of PET in Evaluating the Aging Spine. PET Clin. 2023 Jan;18(1):39–47.
17. Telli T, Desaulniers M, Pyka T, Caobelli F, Forstmann S, Umutlu L, et al. What Role Does PET/MRI Play in Musculoskeletal Disorders? Semin Nucl Med. 2023 Dec 2;S0001-2998(23)00091-0.
18. Biswal S, Behera D, Yoon DH, Holley D, Ith MAM, Carroll I, et al. [18F]FDG PET/MRI of patients with chronic pain alters management: early experience. EJNMMI Phys. 2015 Dec;2(S1):A84, 2197-7364-2-S1-A84.
19. Mostert JM, Oei EHG, Ananta M, Muradin GSR, Huygen FJMP, de Vos CC, et al. (ISMRM 2024) Hybrid Positron Emission Tomography and MRI (PET-MRI) with [18F]FDG for identifying musculoskeletal pain generators: Early experience [Internet]. 2024 [cited 2024 Dec 18]. Available from: https://archive.ismrm.org/2024/4256.html
20. Sawicki LM, Schaarschmidt BM, Heusch P, Buchbender C, Rosenbaum-Krumme S, Umutlu L, et al. Value of ^{18} F-FDG PET/MRI for the outcome of CT-guided facet block therapy in cervical facet syndrome: initial results. J Med Imaging Radiat Oncol. 2017 Jun;61(3):327–33.
21. Weng YS, Tang CT, Chang WC, Huang GS, Chiu CH, Chiang SW, et al. Added value of 18Fluorine-fluorodeoxyglucose (18F-FDG) PET/MRI for evaluation of failed back surgery syndrome: comparison with non-contrast MRI. Jpn J Radiol. 2024 Oct 15;

22. Zhou X, Cipriano P, Kim B, Dhatt H, Rosenberg J, Mittra E, et al. Detection of nociceptive-related metabolic activity in the spinal cord of low back pain patients using 18F-FDG PET/CT. Scand J Pain. 2017 Apr 1;15:53–7.
23. Granger DN, Senchenkova E. Inflammation and the Microcirculation [Internet]. San Rafael (CA): Morgan & Claypool Life Sciences; 2010 [cited 2025 Jun 24]. (Integrated Systems Physiology—From Cell to Function). Available from: http://www.ncbi.nlm.nih.gov/books/NBK53373/
24. Gordon Y, Partovi S, Müller-Eschner M, Amarteifio E, Bäuerle T, Weber MA, et al. Dynamic contrast-enhanced magnetic resonance imaging: fundamentals and application to the evaluation of the peripheral perfusion. Cardiovasc Diagn Ther. 2014 Apr;4(2):147–64.
25. Parker GJM, Roberts C, Macdonald A, Buonaccorsi GA, Cheung S, Buckley DL, et al. Experimentally-derived functional form for a population-averaged high-temporal-resolution arterial input function for dynamic contrast-enhanced MRI. Magn Reson Med. 2006;56(5):993–1000.
26. Cuenod CA, Balvay D. Perfusion and vascular permeability: basic concepts and measurement in DCE-CT and DCE-MRI. Diagn Interv Imaging. 2013 Dec;94(12):1187–204.
27. Tokuda O, Hayashi N, Taguchi K, Matsunaga N. Dynamic contrast-enhanced perfusion MR imaging of diseased vertebrae: analysis of three parameters and the distribution of the time-intensity curve patterns. Skeletal Radiol. 2005 Oct 1;34(10):632–8.
28. Scallan J, Huxley VH, Korthuis RJ. Pathophysiology of Edema Formation. In: Capillary Fluid Exchange: Regulation, Functions, and Pathology [Internet]. Morgan & Claypool Life Sciences; 2010 [cited 2025 Aug 4]. Available from: https://www.ncbi.nlm.nih.gov/books/NBK53445/
29. Gordon Y, Partovi S, Müller-Eschner M, Amarteifio E, Bäuerle T, Weber MA, et al. Dynamic contrast-enhanced magnetic resonance imaging: fundamentals and application to the evaluation of the peripheral perfusion. Cardiovasc Diagn Ther. 2014 Apr;4(2):147–64.
30. Poot DHJ, van der Heijden RA, van Middelkoop M, Oei EHG, Klein S. Dynamic contrast-enhanced MRI of the patellar bone: How to quantify perfusion. J Magn Reson Imaging. 2018 Mar;47(3):848–58.
31. Tofts PS, Brix G, Buckley DL, Evelhoch JL, Henderson E, Knopp MV, et al. Estimating kinetic parameters from dynamic contrast-enhanced T(1)-weighted MRI of a diffusable tracer: standardized quantities and symbols. J Magn Reson Imaging JMRI. 1999 Sep;10(3):223–32.
32. Sourbron SP, Buckley DL. On the scope and interpretation of the Tofts models for DCE-MRI. Magn Reson Med. 2011;66(3):735–45.
33. Sourbron SP, Buckley DL. Classic models for dynamic contrast-enhanced MRI. NMR Biomed. 2013;26(8):1004–27.
34. Biffar A, Sourbron S, Schmidt G, Ingrisch M, Dietrich O, Reiser MF, et al. Measurement of perfusion and permeability from dynamic contrast-enhanced MRI in normal and pathological vertebral bone marrow. Magn Reson Med. 2010;64(1):115–24.
35. Biffar A, Schmidt GP, Sourbron S, D'Anastasi M, Dietrich O, Notohamiprodjo M, et al. Quantitative analysis of vertebral bone marrow perfusion using dynamic contrast-enhanced MRI: Initial results in osteoporotic patients with acute vertebral fracture. J Magn Reson Imaging. 2011 Mar;33(3):676–83.
36. Liu YJ, Huang GS, Juan CJ, Yao MS, Ho WP, Chan WP. Intervertebral Disk Degeneration Related to Reduced Vertebral Marrow Perfusion at Dynamic Contrast-Enhanced MRI. Am J Roentgenol. 2009 Apr;192(4):974–9.
37. Liu YJ, Yang HT, Yao MMS, Lin SC, Cho DY, Shen WC, et al. Quantifying lumbar vertebral perfusion by a Tofts model on DCE-MRI using segmental versus aortic arterial input function. Sci Rep. 2021 Feb 3;11(1):2920.
38. Muftuler LT, Jarman JP, Yu HJ, Gardner VO, Maiman DJ, Arpinar VE. Association between intervertebral disc degeneration and endplate perfusion studied by DCE-MRI. Eur Spine J. 2015 Apr 1;24(4):679–85.
39. Zhang J, Chen Y, Zhang Y, Zhang E, Yu HJ, Yuan H, et al. Diagnosis of spinal lesions using perfusion parameters measured by DCE-MRI and metabolism parameters measured by PET/CT. Eur Spine J Off Publ Eur Spine Soc Eur Spinal Deform Soc Eur Sect Cerv Spine Res Soc. 2020 May;29(5):1061–70.
40. Bhutani M, Turkbey B, Tan E, Korde N, Kwok M, Manasanch EE, et al. Bone marrow abnormalities and early bone lesions in multiple myeloma and its precursor disease: a prospective study using functional and morphologic imaging. Leuk Lymphoma. 2016 May;57(5):1114–21.
41. He X, Zhao L, Guo X, Zhao L, Wu J, Huang J, et al. Differential diagnostic value of 18F-FDG PET/CT for benign and malignant vertebral compression fractures: comparison with magnetic resonance imaging. Cancer Manag Res. 2018 Jul 18;10:2105–15.
42. Seligman L, Kovanlikaya I, Pisapia DJ, Naeger DM, Magge R, Fine HA, et al. Integrated PET-MRI for Glioma Surveillance: Perfusion-Metabolism Discordance Rate and Association With Molecular Profiling. AJR Am J Roentgenol. 2019 Apr;212(4):883–91.

43. Tofts PS. Modeling tracer kinetics in dynamic Gd-DTPA MR imaging. J Magn Reson Imaging. 1997;7(1):91–101.
44. Bäuerle T, Saake M, Uder M. Gadolinium-based contrast agents: What we learned from acute adverse events, nephrogenic systemic fibrosis and brain retention. ROFO Fortschr Geb Rontgenstr Nuklearmed. 2021 Sep;193(9):1010–8.
45. Koninklijk Nederlands Genootschap voor Fysiotherapie (KNGF), Nederlands Huisartsen Genootschap (NHG), Nederlandse Orthopaedische Vereniging (NOV), Nederlandse Vereniging voor Arbeids- en Bedrijfsgeneeskunde (NVAB). Ketenzorgrichtlijn Aspecifieke Lage Rugklachten. 2010.
46. Ross S. Q.Clear [Internet]. GE Healthcare; 2022 [cited 2025 Jun 22]. Available from: https://www.gehealthcare.com/-/media/739d885baa59485aaef5ac0e0eeb44a4.pdf?srsltid=AfmBOoqteJ4Ku534cCa7uvnlYVKpAcuuPl-JpR8j6HM0O-o0T5lney9G
47. Taylor AJ, Salerno M, Dharmakumar R, Jerosch-Herold M. T1 Mapping: Basic Techniques and Clinical Applications. JACC Cardiovasc Imaging. 2016 Jan 1;9(1):67–81.
48. Saranathan M, Rettmann DW, Hargreaves BA, Clarke SE, Vasanawala SS. DIfferential Subsampling with Cartesian Ordering (DISCO): a High Spatio-temporal Resolution Dixon Imaging Sequence for Multiphasic Contrast Enhanced Abdominal Imaging. J Magn Reson Imaging. 2012 Jun;35(6):1484–92.
49. Sacolick LI, Wiesinger F, Hancu I, Vogel MW. B1 Mapping by Bloch-Siegert Shift. Magn Reson Med Off J Soc Magn Reson Med Soc Magn Reson Med. 2010 May;63(5):1315–22.
50. The Mathworks Inc. MATLAB version: 8.6.0 (R2015b) [Internet]. Natick, Massachusetts, United States: The MathWorks Inc.; 2015. Available from: https://www.mathworks.com
51. Yushkevich PA, Piven J, Cody Hazlett H, Gimpel Smith R, Ho S, Gee JC, et al. User-Guided 3D Active Contour Segmentation of Anatomical Structures: Significantly Improved Efficiency and Reliability. Neuroimage. 2006;31(3):1116–28.
52. Klein S, Staring M, Murphy K, Viergever MA, Pluim JPW. elastix: A Toolbox for Intensity-Based Medical Image Registration. IEEE Trans Med Imaging. 2010 Jan;29(1):196–205.
53. Bergen RV, Ryner L, Essig M. Comparison of DCE-MRI parametric mapping using MP2RAGE and variable flip angle T1 mapping. Magn Reson Imaging. 2023 Jan 1;95:103–9.
54. Klein S, Staring M, Murphy K, Viergever MA, Pluim JPW. elastix: A Toolbox for Intensity-Based Medical Image Registration. IEEE Trans Med Imaging. 2010 Jan;29(1):196–205.
55. Unser M. Splines: a perfect fit for signal and image processing. IEEE Signal Process Mag. 1999 Nov;16(6):22–38.
56. de Groot M, Patel N, Manavaki R, Janiczek RL, Bergstrom M, Östör A, et al. Quantifying disease activity in rheumatoid arthritis with the TSPO PET ligand 18F-GE-180 and comparison with 18F-FDG and DCE-MRI. EJNMMI Res. 2019 Dec 19;9(1):113.
57. MacKay JW, Nezhad FS, Rifai T, Kaggie JD, Naish JH, Roberts C, et al. Dynamic contrast-enhanced MRI of synovitis in knee osteoarthritis: repeatability, discrimination and sensitivity to change in a prospective experimental study. Eur Radiol. 2021;31(8):5746–58.
58. Truijman MTB, Kwee RM, van Hoof RHM, Hermeling E, van Oostenbrugge RJ, Mess WH, et al. Combined 18F-FDG PET-CT and DCE-MRI to Assess Inflammation and Microvascularization in Atherosclerotic Plaques. Stroke. 2013 Dec;44(12):3568–70.
59. Boellaard R, Delgado-Bolton R, Oyen WJG, Visser E, Giammarile F, Tatsch K, et al. FDG PET/CT: EANM procedure guidelines for tumour imaging: version 2.0. Eur J Nucl Med Mol Imaging [Internet]. 2014 Jan 1 [cited 2025 Jun 18]; Available from: https://www.academia.edu/24007233/FDG_PET_CT_EANM_procedure_guidelines_for_tumour_imaging_version_2_0
60. Oberg AL, Mahoney DW. Linear Mixed Effects Models. In: Ambrosius WT, editor. Topics in Biostatistics [Internet]. Totowa, NJ: Humana Press; 2007 [cited 2025 Jul 27]. p. 213–34. Available from: https://doi.org/10.1007/978-1-59745-530-5_11
61. Bakdash JZ, Marusich LR. Repeated Measures Correlation. Front Psychol [Internet]. 2017 Apr 7 [cited 2025 Aug 23];8. Available from: https://www.frontiersin.org/journals/psychology/articles/10.3389/fpsyg.2017.00456/full
62. Hellenthal KEM, Brabenec L, Wagner NM. Regulation and Dysregulation of Endothelial Permeability during Systemic Inflammation. Cells. 2022 Jun 15;11(12):1935.
63. Cao Y, Li D, Shen Z, Normolle D. Sensitivity of Quantitative Metrics Derived from DCE MRI and a Pharmacokinetic Model to Image Quality and Acquisition Parameters. Acad Radiol. 2010 Apr;17(4):468–78.

64. Cohen DM, Patel CB, Ahobila-Vajjula P, Sundberg LM, Chacko T, Liu SJ, et al. Blood-Spinal Cord Barrier Permeability in Experimental Spinal Cord Injury: Dynamic Contrast-Enhanced Magnetic Resonance Imaging. NMR Biomed. 2009 Apr;22(3):332–41.
65. Jende JME, Mooshage C, Kender Z, Schimpfle L, Juerchott A, Heiland S, et al. Sciatic nerve microvascular permeability in type 2 diabetes decreased in patients with neuropathy. Ann Clin Transl Neurol. 2022 Apr 30;9(6):830–40.
66. Patel NJ, Gupta V, Vibhute PG, Jain MK, Accurso JM. A Large Cohort Study of 18F Fluoro-Deoxy-Glucose Uptake in Normal Spinal Cord: Quantitative Assessment of the Contamination From Adjacent Vertebral Marrow Uptake and Validity of Normalizing the Cord Uptake Against the Lumbar Thecal Sac. J Comput Assist Tomogr. 2017 Jan;41(1):125–30.
67. Galle J, Quaschning T, Seibold S, Wanner C. Endothelial dysfunction and inflammation: What is the link? Kidney Int. 2003 May 1;63:S45–9.
68. Tomlinson RE, Silva MJ. Skeletal Blood Flow in Bone Repair and Maintenance. Bone Res. 2013 Dec;1(1):311–22.
69. Rajasekaran S, Babu JN, Arun R, Armstrong BRW, Shetty AP, Murugan S. ISSLS Prize Winner: A Study of Diffusion in Human Lumbar Discs: A Serial Magnetic Resonance Imaging Study Documenting the Influence of the Endplate on Diffusion in Normal and Degenerate Discs. Spine. 2004 Dec 1;29(23):2654.
70. Miese F, Scherer A, Ostendorf B, Heinzel A, Lanzman RS, Kröpil P, et al. Hybrid 18F-FDG PET–MRI of the hand in rheumatoid arthritis: initial results. Clin Rheumatol. 2011 Sep 1;30(9):1247–50.
71. Urban JPG, Smith S, Fairbank JCT. Nutrition of the Intervertebral Disc. Spine. 2004 Dec 1;29(23):2700.
72. Li H, Yan J zhi, Chen Y jie, Kang W bo, Huang J xi. Non-invasive quantification of age-related changes in the vertebral endplate in rats using in vivo DCE-MRI. J Orthop Surg. 2017 Nov 9;12(1):169.
73. Haro H, Kato T, Komori H, Osada M, Shinomiya K. Vascular endothelial growth factor (VEGF)-induced angiogenesis in herniated disc resorption. J Orthop Res Off Publ Orthop Res Soc. 2002 May;20(3):409–15.
74. Fournier DE, Kiser PK, Shoemaker JK, Battié MC, Séguin CA. Vascularization of the human intervertebral disc: A scoping review. JOR Spine. 2020 Sep 15;3(4):e1123.
75. Keorochana G, Taghavi CE, Tzeng ST, Lee KB, Liao JC, Yoo JH, et al. MRI classification of interspinous ligament degeneration of the lumbar spine: intraobserver and interobserver reliability and the frequency of disagreement. Eur Spine J. 2010 Oct 1;19(10):1740–5.
76. Strittmatter A, Caroli A, Zöllner FG. A Multistage Rigid-Affine-Deformable Network for Three-Dimensional Multimodal Medical Image Registration. Appl Sci. 2023 Jan;13(24):13298.
77. Raiten DJ, Ashour FAS, Ross AC, Meydani SN, Dawson HD, Stephensen CB, et al. Inflammation and Nutritional Science for Programs/Policies and Interpretation of Research Evidence (INSPIRE)12345. J Nutr. 2015 May;145(5):1039S-1108S.

Acknowledgements

First and foremost, I would like to extend my sincere thanks to my dedicated supervisors. To my daily supervisor Marijn, thank you for your dedication, patience, and friendliness. Thanks for bringing me to Jong Erasmus drinks and introducing me to many friendly people. It has been a such pleasure working with you, and I wish you the best of luck completing the AMPHiBI trial and your PhD course. To my medical supervisor Rianne, thank you for keeping me focused on the clinical goal, and thanks especially for your personal trust in me when I was lacking confidence. Last but not least, thanks to my technical supervisor Dirk for sharing your technical expertise with me. I have learned countless lessons from each three of you.

Thanks also to Jie, Yijie, Huib, Daniek and other colleagues in and around the Ca-316 Office. It has been a pleasure getting to know all of you and I am grateful for your kindness in listening to my regular struggles.

Many thanks, love and mutual support go out to my parents and sisters. You have supported me in so many ways over the course of my studies. The past few months have been incredibly challenging for us and I am grateful to know that we can lean on one another, even when it does not come easily. This is also for my grandparents, whom I thought of often during this process. Four years ago, the last good news I could share with Grandma was that I would start my master's degree after the summer. I find comfort in the thought that you would have been very proud of me.

Finally, a heartfelt thanks to my roommates Britt and Leonie, for your closeness or space, and for understanding which I needed during this past time. Arnau, thank you for your companionship from such a long distance; you are one of the best listeners I know. Many happy thanks to all of my friends who have the past eight years at university such an incredible, enjoyable, educational, colorful, musical, crazy, unforgettable time.

Josefien van den Berg
Rotterdam, August 2025

Appendix

A) AMPHiBI trial inclusion and exclusion criteria

Inclusion criteria

- Age between 18 and 75 years
- Persisting pain, defined as (more than 3 months)
    - Hip patient specific
        - pain in the hip region after ipsilateral hip prosthesis more than 10 months ago
        - patients must report an NRS scale of 3 or higher
    - Low back group specific:
        - no improvement of symptoms after at least three months of conservative treatment according to the Dutch guidelines for non-specific low back pain (GP care (advise to stay active and pain medication) and exercise therapy) in primary care.
        - patients must report an NRS scale of 6 or higher
        - in case of prior surgery: at least 10 months ago
- Eligible to undergo ^{18}F-FDG PET/MRI
- Capable to participate in the study

Exclusion criteria

- Contra-indications for ^{18}F-FDG PET/MRI (e.g. metallic foreign bodies, etc.)
- Known renal insufficiency
- Known allergy to contrast agents
- Prior spinal fusion
- BMI >35 kg/m2
- Cancer
- Opioid addiction
- Metabolic disorders
- Neurodegenerative disorders
- Psychiatric disorders or severe psychological problems
- Anti-coagulation with vital medical indication

NRS = numeric rating scale
^{18}F-FDG PET/MRI = ^{18}F-Fluorodeoxyglucose positron emission tomography/magnetic resonance imaging
GP = general practitioner
BMI = body mass index

B) Repeated measures correlation matrices

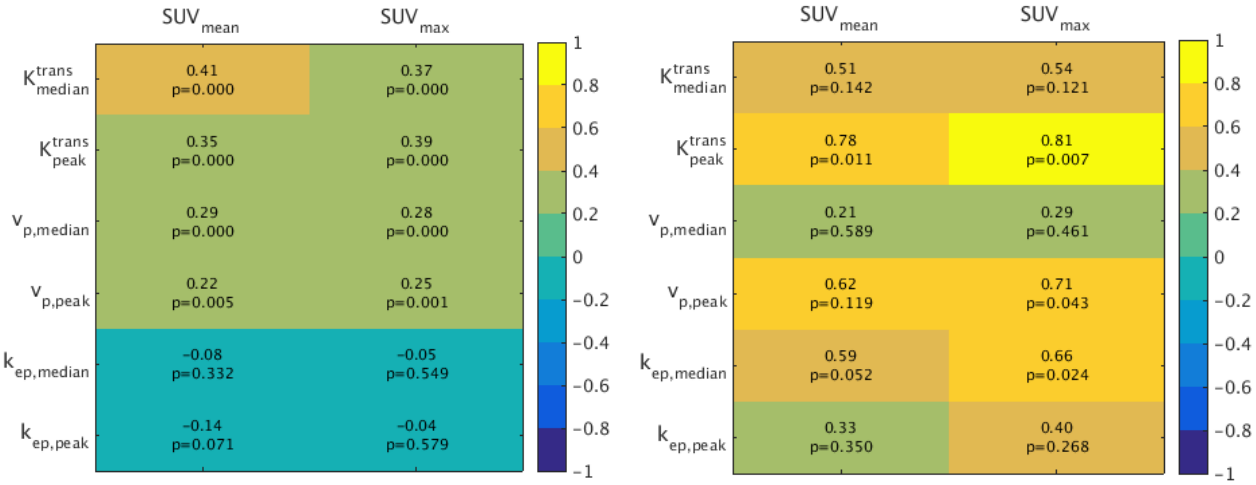

Repeated-measures correlation matrix (rmcorr) on ranked data in all regions of interest combined (left) and spinal canal (right).
SUV: standardized uptake value

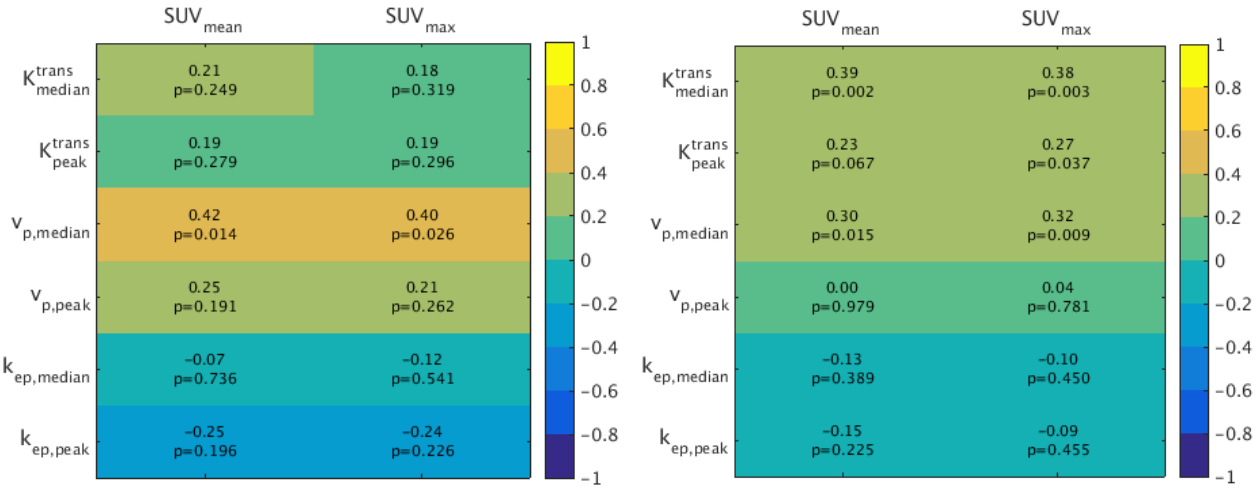

Repeated-measures correlation matrix (rmcorr) on ranked data in the nerve root (left) and facet joint (right).
SUV: standardized uptake value

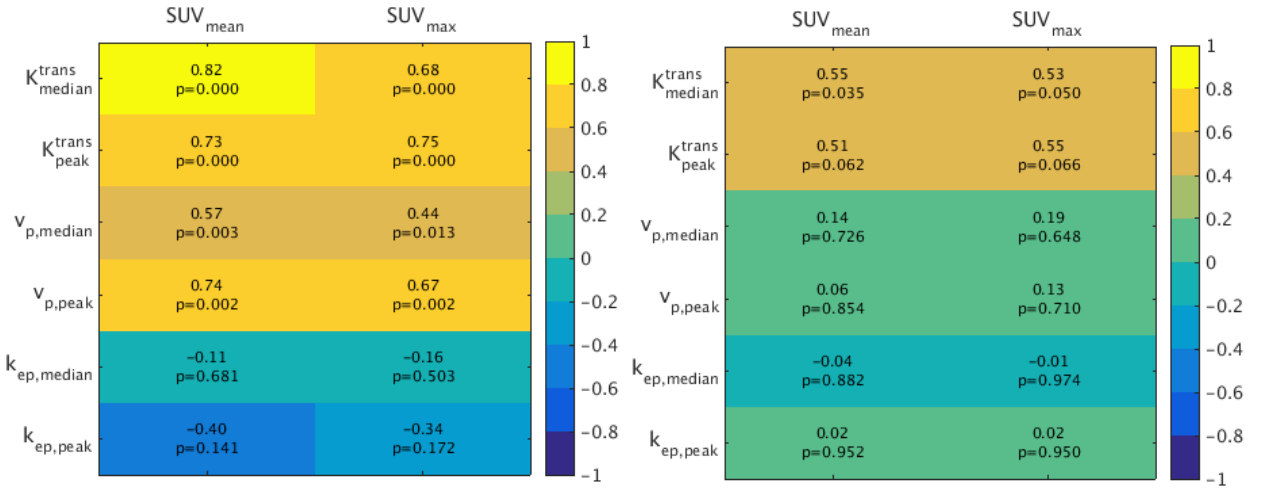

Repeated-measures correlation matrix (rmcorr) on ranked data in the intervertebral disc (left) and interspinous tissue (right).
SUV: standardized uptake value

C) Literature review

Evaluating Inflammation in the Spine with [18F]FDG-PET and Contrast-Enhanced MRI

Josefien van den Berg
TM30001
07/02/2025

Abstract

Chronic back pain is a prevalent condition associated with a high disease burden globally. Anatomical imaging often fails to adequately pinpoint the pain source. Low-grade inflammation may be a part of the pathophysiology or a consequence of pain. Functional imaging techniques, such as 18F-fluorodeoxyglucose positron emission tomography ([18F]FDG-PET) and dynamic contrast enhanced magnetic resonance imaging (DCE-MRI), offer insights into metabolic and microcirculatory changes that may be indicative of inflammation and pain. However, the relation between quantitative metrics of FDG uptake and (dynamic) contrast enhancement as surrogate markers of inflammation is unknown, leaving the question if both PET and DCE modalities are necessary. This review examines the roles of [18F]FDG-PET and (dynamic) CE-MRI in evaluating spinal pain, and their correlation in evaluating inflammation.

Introduction

Chronic back pain is a prevalent condition associated with a high disease burden globally (1). Magnetic resonance imaging (MRI) is often used in patients with longstanding back pain due to its high resolution and anatomic detail (2–4). However, assessment of MRI images remains ambiguous, as signal characteristics and structural features show no to weak associations to pain and lack specificity, because structural abnormalities can also be prevalent in asymptomatic patients (3,5–8). Without an identified pain source, therapies lack a treatment target and are often inadequate, with the risk of unnecessary surgeries and overuse of opioids (5,9).

As anatomical imaging fails to adequately pinpoint pain generators, recent research has shifted its focus to functional imaging techniques. 18-Fluorodeoxyglucose positron emission tomography ([18F]FDG-PET) measures tissue glycolysis and is commonly used for detection of tumors or infections. Glucose metabolism is also increased in early stages of inflammation (9,10), and low-grade inflammation may be an element of the pathophysiology or a consequence of chronic pain conditions (11,12). Therefore, [18F]FDG-PET could be a useful method to detect inflammation in the context of pain. Similarly, chronically inflamed tissues display hypervascularization to meet the increased oxygen demand. Contrast-enhanced MRI (CE-MRI) is able to evaluate perfusion by imaging paramagnetic contrast agents in a tissue, revealing physiological changes of microcirculation (13). Heuristic and pharmacokinetic parameters of dynamic contrast-enhanced (DCE) MRI reflect vascular and cellular properties of a tissue by tracking the contrast agent through repeated scans of the same tissue (13,14).

Combined [18F]FDG-PET and (dynamic) CE-MRI could complement one another by integrating glucose metabolism and perfusion measurements to identify the source of chronic pain (2,9,15,16). The potential of hybrid [18F]FDG-PET/MRI to reveal previously unidentified pain generators has already been shown (2,17–19). However, it is unknown whether PET/MRI and CE-MRI are complementary techniques, or if either modality is redundant. Moreover, the relation between quantitative metrics of FDG uptake and (dynamic) contrast enhancement as surrogate markers of inflammation has not been studied.

This review examines the roles of [18F]FDG-PET and (dynamic) CE-MRI in evaluating spinal pain. The primary focus is on chronic pain, with secondary discussions on inflammatory diseases, infection and oncology. The literature search was conducted primarily via PubMed and EMBASE using a combination of key terms, including “contrast-enhanced MRI”, “[18F]FDG-PET”, “spine”, “pain”, “inflammation”, and their derivatives. In addition to the database searches, citation chaining was employed to identify relevant articles referenced in the initial retrieved papers.

Pain

Back pain is attributed to the intervertebral disc in most cases, followed by the facet joint and sacroiliac joint (SIJ) (20). Other causes of pain are related to the nerves, compression fractures or microfractures, inflammatory arthropathies, infections, and primary or metastasized tumors (5,21).

Neuropathy

Neuronal activity in the spinal cord requires glucose metabolism (22). In the painful spine, metabolic demand may be increased due to hypersensitivity of neurons by long-term nociceptive stimuli (23). In a study by Zhou et al. (24), subjects with low back pain showed higher values of normalized maximal

standardized uptake value (SUV_{max}) on [18F]FDG PET/CT in the spinal canal at vertebral levels T7 to T10 than the control group. The authors stated that the increased FDG uptake observed may not only result from inflammation but could also reflect heightened neurosensory and neuromotor activity in the spinal cord levels associated with lower back pain (24).

Pain from an impinged or damaged nerve is thought to trigger a neuroinflammatory response (15). The resulting hypermetabolism can be traced using [18F]FDG and complement MRI imaging, which has a low specificity for identifying the source of radicular pain (21). Indeed, the combination of FDG-PET and unenhanced MRI has shown increased diagnostic accuracy in chronic pain patients compared to MRI or PET alone (4,17), although the numbers of subjects in these studies were small. In the study by Cipriano et al. (4), five patients with spinal nerve impingement due to a herniated disc showed a higher SUV_{max} in the lateral recess of the painful side compared to the asymptomatic contralateral side. Increased FDG uptake is also correlated with discomfort in patients with failed back surgery (FBS), where nerve root or peripheral nerve entrapment are common pain sources (2,25). In a case study, the elevated uptake was seen in an epidural scar that caused entrapment neuropathy (25).

CE-MRI was not performed in studies of neuropathic pain (2,4,17,25), so visual and quantitative parameters of (dynamic) enhancement in the spinal cord or quantitative parameters remain unknown. Perfusion of peripheral nerves at thigh level with DCE magnetic resonance neurography has been investigated by Jende et al. (26) in type II diabetic patients. They found that capillary permeability (K^{trans}) and the volume fraction of the extravascular extracellular space (v_e) in the sciatic nerve were decreased in diabetic patients with neuropathy compared to those without neuropathy (26). Although this study focused on peripheral nerves, applying similar perfusion assessments to nociceptive and neuropathic lesions in the spinal canal with DCE-MRI could be a promising direction for future research.

Osteoarthritis

Osteoarthritis (OA) was traditionally viewed as a wear-and-tear disease of cartilage, but is now increasingly understood as a complex whole-joint disease involving cartilage, bone, and synovium. OA is associated with pain, and low-grade inflammation plays a significant role in its pathophysiology and progression (3,21,27).

Degenerative changes of the facet joint or intervertebral disc in OA can lead to high focal activity on [18F]FDG-PET (5,19,21,28,29). Facet arthropathy can be detected by increased FDG uptake in the painful facet joint (4,19). In two patients with chronic back pain, increased FDG uptake corresponded with the pain location in the L5-S1 facet joint due to arthropathy in one patient, and the L5 pars interarticularis due to spondylolysis in the other (4). Joint arthropathy is also a painful complication of failed back surgery. Elevated FDG uptake in the facet joint contributed to recognizing facet arthropathy as the pain source in five FBS patients, thereby increasing diagnostic accuracy of [18F]FDG-PET/MRI compared to non-contrast MRI alone (2). FDG uptake has been shown in intervertebral discs, spinous processes and facet joints in the aging spine, suggesting inflammation plays a role in the degenerative process (29,30), but more research is needed to confirm the value of PET for OA of the spine (28).

D'Aprile et al. (31) investigated the performance of contrast imaging in degeneration of the lumbar spine. Here, 987 out of 2820 patients received intravenous Gd contrast because conventional MRI

could not detect osteoarticular and/or musculoligamentous edema to pinpoint the pain source. From these 987 patients, CE findings could either improve lesion evaluation (80%) or identify the pain source missed from previous images (11%). Apart from improved diagnostic performance based on the finding of disc degeneration, CE-MRI can identify bone marrow changes, discitis, synovitis, microfractures in spondylolysis, and ligamentous stress (31). Dynamic CE-MRI has shown a positive relation between the area under the contrast enhancement curve and disc degeneration in the cartilaginous endplates and subchondral bone (32). This may be due to disruption of the integrity of the bone, even from microscopic damages that precede macroscopic changes (32).

Beside disc and bone degeneration, synovitis is an important feature of OA (21,33) and is strongly related to pain severity (34). [18F]FDG-PET and CE-MRI have demonstrated utility in assessing synovitis in OA, although most research focused on peripheral joints rather than the spine (3). The rate of early enhancement is positively related to microscopic inflammation in the synovial membrane of OA knees (35). Similarly, FDG uptake was significantly elevated in the synovium and middle joint space of painful knees compared to asymptomatic knees (36). The co-localization of increased CE-MRI and PET parameters in the synovium of painful joints may suggest a positive correlation between these imaging biomarkers in OA.

Combining [18F]FDG and DCE modalities, Lehman et al. (37) showed the added value of contrast enhancement in hybrid PET/MRI imaging in 10 patients with lumbar facet joint pain. MRI images were scored visually based on T2 hyperintensity or enhancement in osseous tissue, and edema or enhancement in soft tissues. When assessing contrast enhanced images compared to non-contrast MRI, the number of identified facet joints increased as well as their MRI scores. Furthermore, increased FDG activity was highly correlated with high MRI scores (37). This could suggest a correlation between FDG uptake and contrast enhancement in these patients, although the authors did not make a direct comparison of the contrast and FDG results.

While the diagnostic value of [18F]FDG-PET and (CE) MRI for neuropathic and low-grade inflammatory spinal pain conditions has been shown, previous studies have not yet investigated quantitative metrics available from each modality. Given the limited research in this area and the idea that chronic pain may be driven by low-grade inflammation, this review expands its focus to inflammatory diseases, which may serve as a model for exploring quantitative parameters of PET/MRI in chronic pain generators. After all, inflammatory diseases are often associated with pain.

Inflammatory diseases

Spondyloarthritis

Spondyloarthritis (SpA) is a family of inflammatory rheumatic diseases. Chronic back pain is the most important symptom (38–40). Ankylosing spondylitis (AS) is a type of arthritis causing inflammation in the spinal joints and ligaments and is a key presentation of axial SpA, whereas peripheral spondyloarthritis includes psoriatic arthritis, reactive arthritis, arthritis associated with inflammatory bowel disease, and undifferentiated peripheral SpA (38,39,41). Despite some overlap between axial and peripheral spondyloarthritis, and the peripheral subtypes may also show axial involvement (39), this review limits its focus of rheumatic disease to axial SpA. As SpA involves inflammation of the joints, diagnostic imaging can target such inflammatory patterns (39).

Conventional MRI is commonly used to diagnose axial SpA, with T2-weighted or short tau inversion recovery sequences effectively detecting bone marrow edema (BME) as a sign of osteitis in the axial skeleton, though BME is not specific to axial SpA (40,42,43). Other inflammatory lesions of axial SpA include synovitis, enthesitis and capsulitis in the SIJ; and spondylitis, facet joint inflammation, and aseptic spondylodiscitis in the spine (40,44). These entities show increased vascularization, and can therefore be detected by Gd contrast sequences (40,42,45). [18F]FDG-PET is not routinely used in the assessment of ankylosing spondylitis, but a recent study has shown a strong correlation between FDG uptake in affected joints and disease activity in AS (46). FDG uptake can be traced to the intervertebral discs, as aseptic spondylodiscitis is a common feature of AS (47).

Rheumatoid arthritis

Rheumatoid arthritis (RA) is a multisystemic inflammatory disease that affects the musculoskeletal system, especially synovial joints. It is characterized by erosive synovitis and the most important symptom is pain (21,39). While RA rarely involves the back, the spine is also made up of synovial joints, so imaging peripheral joint inflammation in RA may serve as a model for imaging spinal inflammation.

Many rheumatic diseases show distinct [18F]FDG uptake patterns, making PET a useful modality for diagnosis and disease monitoring (39). For example, FDG uptake is elevated in the synovium in peripheral RA joints (48–50). Similarly, gadolinium contrast can also detect synovitis and bone erosions and identify active inflammation (15). Synovial inflammation in RA knees show a high rate of early enhancement on DCE-MRI (35). Sites of increased contrast enhancement correspond with increased FDG uptake in synovitis and tenosynovitis (51). Furthermore, parameters of (dynamic) CE-MRI (K^{trans}, initial rate of enhancement, maximal enhancement, volume of enhancing pannus) and PET (SUV_{max}) have shown a strong positive correlation in the synovial spaces of symptomatic wrists and slightly weaker in the hands (52). The modalities could therefore be close surrogates, and the use of a single technique may be sufficient for RA assessment.

Infection

Spondylodiscitis, discitis, and vertebral osteomyelitis are spinal infections located in specific spinal tissues. MRI is considered the most accurate modality for early detection of spondylodiscitis (53). Gadolinium enhancement may be seen parallel to the endplate in early stages of the disease, and later in the entire vertebral body and disc (54). [18F]FDG is known to show increased uptake in infections, and has been shown to differentiate infectious endplate from degenerative changes found on MRI (55). Many studies have indicated the added value of combined [18F]FDG-PET and CE-MRI in the diagnosis of osteomyelitis in the spine (10,56–60). In the prospective study by Fuster et al. (57), the agreement between CE-MRI and PET/CT for the diagnosis of spondylodiscitis was poor. This could suggest the complementary roles of both modalities as they detect different physiological features of the infected tissue. This hypothesis is supported by Paez et al. (59), who also demonstrated the highest diagnostic performance when combining PET and MRI. Unfortunately, specific results of contrast enhancement, e.g. number and location of enhancing regions, were not investigated, nor their correlation to [18F]FDG uptake.

Oncology

To our knowledge, Zhang et al. (16) are the only authors who have directly evaluated the association between quantitative parameters as measured by DCE-MRI and [18F]FDG-PET/CT in spinal lesions.

They manually placed a region of interest (ROI) of 0.5-1.2 cm^2 on an area showing strong gadolinium enhancement, or the entire area showing high FDG uptake. They found no significant association between K^{trans} and/or exchange rate constant (k_{ep}) and SUV_{max} in malignant, benign and borderline spinal tumors, implying that blood perfusion and glucose metabolism were not directly related. This suggests that DCE-MRI and PET may provide complementary information for patients with spinal tumors, reflecting different aspects of the lesions (16).

Discussion

By providing markers of glucose metabolism and microcirculation, [18F]FDG-PET and DCE-MRI may reflect different aspects of inflammation. The combined modalities have shown good diagnostic value in neuropathy, disc degeneration, inflammatory diseases, infection and oncology. There is no unequivocal correlation between the parameters among these diseases. While the parameters were not correlated in spinal tumor lesions, suggesting complementary values, they showed a strong positive correlation in rheumatic joints, meaning they could be close surrogates. However, there is a lack of understanding of the relation of these parameters in the context of chronic pain.

Hybrid PET/MRI systems were introduced to the clinic around a decade ago, although not yet in widespread use due to high costs and time consumption (21). Furthermore, the clinical implementation of molecular imaging and dynamic contrast imaging has gained more popularity in the oncological domain than inflammatory or pain-related indications (37). These reasons may explain the scarcity of research on quantitative PET/MRI in chronic back pain. The potential of hybrid PET/MRI to reveal previously unidentified pain generators has recently been shown (2,17–19), but no research exists yet that correlates quantitative parameters of PET and DCE in spinal pain sources. This creates an opportunity for future research.

Direct quantitative correlations between DCE and PET parameters are seldom reported in literature as most studies focus on diagnostic outcomes. Zhang et al. (16) have compared the PET and DCE data based on manually placed ROIs on tumor lesions (up to 1.2 cm^2 on DCE or entire region on PET). However, averaging parameters over an ROI may result in loss of information, especially in heterogeneous lesions. To account for this, the correlation between DCE and FDG could also be studied by a voxel-by-voxel analysis. Besson et al. (61) were the first to make a voxel-wise correlative analysis of simultaneous [18F]FDG-PET/DCE-MRI data in non-small-cell lung tumors (61). Simultaneous acquisition in hybrid PET/MRI offers improved spatial registration compared to sequential imaging, because there is no different positioning between scans, and simultaneous data acquisition is less affected by patient movement or involuntary organ movement (62). However, errors in DCE pharmacokinetic modeling and motion correction could still occur and reduce the reliability of these results. Indeed, in the study by Besson et al. (61), the relative root mean square errors for PET and DCE curve fittings were 10.3% and 31.8%, respectively, and were attributed to motion corruption. Voxel-wise approaches are especially sensitive to motion artifacts and noise (63). Gaussian smoothing was applied to denoise PET data and smooth motion-corrupted time-varying activity curves (61). Since the spatial distribution of vascularization and perfusion properties in pain generators is unknown, future research could investigate both ROI and voxel-wise correlations.

Conclusion

This review addresses the potential of combined [18F]FDG-PET and (D)CE-MRI for assessing inflammation and pain in the spine. The combination of PET and MRI outperforms each separate

modality in terms of diagnostic accuracy in neuropathy, osteoarthritis and spinal infections. Quantitative parameters reflecting glucose metabolism and microcirculation seem to be correlated in joint arthropathies, but not in infections and tumor lesions. However, direct quantitative correlations in chronic back pain generators remain to be investigated.

References

1. Rubin DI. Epidemiology and Risk Factors for Spine Pain. Neurol Clin. 2007 May;25(2):353–71.
2. Weng YS, Tang CT, Chang WC, Huang GS, Chiu CH, Chiang SW, et al. Added value of 18Fluorine-fluorodeoxyglucose (18F-FDG) PET/MRI for evaluation of failed back surgery syndrome: comparison with non-contrast MRI. Jpn J Radiol. 2024 Oct 15;
3. Kogan F, Yoon D, Teeter MG, Chaudhari AJ, Hales L, Barbieri M, et al. Multimodal positron emission tomography (PET) imaging in non-oncologic musculoskeletal radiology. Skeletal Radiol [Internet]. 2024 Mar 16 [cited 2024 Apr 3]; Available from: https://link.springer.com/10.1007/s00256-024-04640-4
4. Cipriano PW, Yoon D, Gandhi H, Holley D, Thakur D, Hargreaves BA, et al. ^{18} F-FDG PET/MRI in Chronic Sciatica: Early Results Revealing Spinal and Nonspinal Abnormalities. J Nucl Med. 2018 Jun;59(6):967–72.
5. Lehman VT, Tiegs-Heiden CA, Broski SM. Beyond Anatomy: Fat-Suppressed MR and Molecular Imaging of Spinal Pain Generators. Radiol Clin North Am. 2024 Mar;62(2):247–61.
6. Jensen MC, Brant-Zawadzki MN, Obuchowski N, Modic MT, Malkasian D, Ross JS. Magnetic resonance imaging of the lumbar spine in people without back pain. N Engl J Med. 1994 Jul 14;331(2):69–73.
7. el Barzouhi A, Vleggeert-Lankamp CLAM, Lycklama à Nijeholt GJ, Van der Kallen BF, van den Hout WB, Jacobs WCH, et al. Magnetic resonance imaging in follow-up assessment of sciatica. N Engl J Med. 2013 Mar 14;368(11):999–1007.
8. Carragee EJ, Alamin TF, Miller JL, Carragee JM. Discographic, MRI and psychosocial determinants of low back pain disability and remission: a prospective study in subjects with benign persistent back pain. Spine J. 2005 Jan 1;5(1):24–35.
9. Yoon D, Kogan F, Gold GE, Biswal S. Identifying Musculoskeletal Pain Generators Using Clinical PET. Semin Musculoskelet Radiol. 2020 Aug;24(4):441–50.
10. Smids C, Kouijzer IJE, Vos FJ, Sprong T, Hosman AJF, de Rooy JWJ, et al. A comparison of the diagnostic value of MRI and 18F-FDG-PET/CT in suspected spondylodiscitis. Infection. 2017;45(1):41–9.
11. Bäckryd E, Lind AL, Thulin M, Larsson A, Gerdle B, Gordh T. High levels of cerebrospinal fluid chemokines point to the presence of neuroinflammation in peripheral neuropathic pain: a cross-sectional study of 2 cohorts of patients compared with healthy controls. Pain. 2017 Dec;158(12):2487–95.
12. Moen A, Lind AL, Thulin M, Kamali-Moghaddam M, Røe C, Gjerstad J, et al. Inflammatory Serum Protein Profiling of Patients with Lumbar Radicular Pain One Year after Disc Herniation. Int J Inflamm. 2016;2016:3874964.
13. Cuenod CA, Balvay D. Perfusion and vascular permeability: basic concepts and measurement in DCE-CT and DCE-MRI. Diagn Interv Imaging. 2013 Dec;94(12):1187–204.
14. Gordon Y, Partovi S, Müller-Eschner M, Amarteifio E, Bäuerle T, Weber MA, et al. Dynamic contrast-enhanced magnetic resonance imaging: fundamentals and application to the evaluation of the peripheral perfusion. Cardiovasc Diagn Ther. 2014 Apr;4(2):147–64.
15. Kogan F, Broski SM, Yoon D, Gold GE. Applications of PET-MRI in musculoskeletal disease: PET-MRI of MSK Disease. J Magn Reson Imaging. 2018 Jul;48(1):27–47.
16. Zhang J, Chen Y, Zhang Y, Zhang E, Yu HJ, Yuan H, et al. Diagnosis of spinal lesions using perfusion parameters measured by DCE-MRI and metabolism parameters measured by PET/CT. Eur Spine J Off Publ Eur Spine Soc Eur Spinal Deform Soc Eur Sect Cerv Spine Res Soc. 2020 May;29(5):1061–70.
17. Biswal S, Behera D, Yoon DH, Holley D, Ith MAM, Carroll I, et al. [18F]FDG PET/MRI of patients with chronic pain alters management: early experience. EJNMMI Phys. 2015 Dec;2(S1):A84, 2197-7364-2-S1-A84.
18. Mostert JM, Oei EHG, Ananta M, Muradin GSR, Huygen FJMP, de Vos CC, et al. (ISMRM 2024) Hybrid Positron Emission Tomography and MRI (PET-MRI) with [18F]FDG for identifying musculoskeletal pain generators: Early experience [Internet]. 2024 [cited 2024 Dec 18]. Available from: https://archive.ismrm.org/2024/4256.html
19. Sawicki LM, Schaarschmidt BM, Heusch P, Buchbender C, Rosenbaum-Krumme S, Umutlu L, et al. Value of ^{18} F-FDG PET/MRI for the outcome of CT-guided facet block therapy in cervical facet syndrome: initial results. J Med Imaging Radiat Oncol. 2017 Jun;61(3):327–33.

20. DePalma MJ, Ketchum JM, Saullo T. What Is the Source of Chronic Low Back Pain and Does Age Play a Role? Pain Med. 2011 Feb;12(2):224–33.
21. Telli T, Desaulniers M, Pyka T, Caobelli F, Forstmann S, Umutlu L, et al. What Role Does PET/MRI Play in Musculoskeletal Disorders? Semin Nucl Med. 2023 Dec 2;S0001-2998(23)00091-0.
22. Schadrack J, Neto FL, Ableitner A, Castro-Lopes JM, Willoch F, Bartenstein P, et al. Metabolic activity changes in the rat spinal cord during adjuvant monoarthritis. Neuroscience. 1999 Sep 1;94(2):595–605.
23. Woolf CJ, Salter MW. Neuronal plasticity: Increasing the gain in pain. Science. 2000;288(5472):1765–8.
24. Zhou X, Cipriano P, Kim B, Dhatt H, Rosenberg J, Mittra E, et al. Detection of nociceptive-related metabolic activity in the spinal cord of low back pain patients using 18F-FDG PET/CT. Scand J Pain. 2017 Apr 1;15:53–7.
25. Tsai YH, Huang GS, Tang CT, Chang WC, Hsu YC. Case Report: Nerve Root Entrapment Due to Epidural Fibrosis in a Patient With Failed Back Surgery Syndrome: Value of 2-18F-Fluorodeoxyglucose Simultaneous Positron Emission Tomography-Magnetic Resonance Imaging. Front Med. 2022 Apr 25;9:860545.
26. Jende JME, Mooshage C, Kender Z, Schimpfle L, Juerchott A, Heiland S, et al. Sciatic nerve microvascular permeability in type 2 diabetes decreased in patients with neuropathy. Ann Clin Transl Neurol. 2022 Apr 30;9(6):830–40.
27. Berenbaum F. Osteoarthritis as an inflammatory disease (osteoarthritis is not osteoarthrosis!). Osteoarthritis Cartilage. 2013 Jan;21(1):16–21.
28. Katal S, Clifford TG, Matcuk G, Eibschutz L, Gholamrezanezhad A. Clinical Applications of PET in Evaluating the Aging Spine. PET Clin. 2023 Jan;18(1):39–47.
29. Rosen RS, Fayad L, Wahl RL. Increased 18F-FDG Uptake in Degenerative Disease of the Spine: Characterization with 18F-FDG PET/CT. J Nucl Med. 2006 Aug 1;47(8):1274–80.
30. Aliyev A, Saboury B, Kwee TC, Torigian DA, Basu S, Christensen HW, et al. Age-related inflammatory changes in the spine as demonstrated by 18F-FDG-PET: Observation and insight into degenerative spinal changes. Hell J Nucl Med. 2012;15(3):197-201+268.
31. D'Aprile P, Nasuto M, Tarantino A, Guglielmi G, Jinkins JR, Cornacchia S. Magnetic Resonance Imaging in degenerative disease of the lumbar spine: Fat Saturation technique and contrast medium. Acta Biomed Atenei Parm. 2018 Jan 19;89(1-S):208–19.
32. Muftuler LT, Jarman JP, Yu HJ, Gardner VO, Maiman DJ, Arpinar VE. Association between intervertebral disc degeneration and endplate perfusion studied by DCE-MRI. Eur Spine J. 2015 Apr 1;24(4):679–85.
33. Hayashi D, Roemer FW, Katur A, Felson DT, Yang SO, Alomran F, et al. Imaging of Synovitis in Osteoarthritis: Current Status and Outlook. Semin Arthritis Rheum. 2011 Oct;41(2):116–30.
34. Baker K, Grainger A, Niu J, Clancy M, Guermazi A, Crema M, et al. Relation of synovitis to knee pain using contrast-enhanced MRIs. Ann Rheum Dis. 2010 Oct 1;69(10):1779–83.
35. Østergaard M, Stoltenberg M, Løvgreen-Nielsen P, Volck B, Sonne-Holm S, Lorenzen I. Quantification of synovitis by MRI: correlation between dynamic and static gadolinium-enhanced magnetic resonance imaging and microscopic and macroscopic signs of synovial inflammation. Magn Reson Imaging. 1998 Sep;16(7):743–54.
36. Parsons MA, Moghbel M, Saboury B, Torigian DA, Werner TJ, Rubello D, et al. Increased FDG uptake suggests synovial inflammatory reaction with osteoarthritis: preliminary in vivo results in humans. Nucl Med Commun. 2015 Dec;36(12):1215–9.
37. Lehman VT, Diehn FE, Broski SM, Nathan MA, Kemp BJ, Larson NB, et al. Comparison of [^{18} F] FDG-PET/MRI and Clinical Findings for Assessment of Suspected Lumbar Facet Joint Pain: A Prospective Study to Characterize Candidate Nonanatomic Imaging Biomarkers and Potential Impact on Management. Am J Neuroradiol. 2019 Sep 26;ajnr;ajnr.A6224v1.
38. Arnbak B, Leboeuf-Yde C, Jensen TS. A systematic critical review on MRI in spondyloarthritis. Arthritis Res Ther. 2012;14(2):R55.
39. Hotta M, Minamimoto R, Kaneko H, Yamashita H. Fluorodeoxyglucose PET/CT of Arthritis in Rheumatic Diseases: A Pictorial Review. RadioGraphics. 2020 Jan;40(1):223–40.
40. Khmelinskii N, Regel A, Baraliakos X. The Role of Imaging in Diagnosing Axial Spondyloarthritis. Front Med. 2018 Apr 17;5:106.
41. Branch NSC and O. National Institute of Arthritis and Musculoskeletal and Skin Diseases. NIAMS; 2017 [cited 2025 Jan 24]. Arthritis and Rheumatic Diseases. Available from: https://www.niams.nih.gov/health-topics/arthritis-and-rheumatic-diseases
42. de Hooge M, van den Berg R, Navarro-Compán V, van Gaalen F, van der Heijde D, Huizinga T, et al. Magnetic resonance imaging of the sacroiliac joints in the early detection of spondyloarthritis: no added value of

gadolinium compared with short tau inversion recovery sequence. Rheumatology. 2013 Jul 1;52(7):1220–4.
43. Weber U, Hodler J, Kubik RA, Rufibach K, Lambert RGW, Kissling RO, et al. Sensitivity and specificity of spinal inflammatory lesions assessed by whole-body magnetic resonance imaging in patients with ankylosing spondylitis or recent-onset inflammatory back pain. Arthritis Care Res. 2009;61(7):900–8.
44. Hermann KGA, Baraliakos X, van der Heijde DM, Jurik AG, Landewé R, Marzo-Ortega H, et al. Descriptions of spinal MRI lesions and definition of a positive MRI of the spine in axial spondyloarthritis: a consensual approach by the ASAS/OMERACT MRI study group. Ann Rheum Dis. 2012 Aug 1;71(8):1278–88.
45. Hermann KGA, Baraliakos X, van der Heijde DM, Jurik AG, Landewé R, Marzo-Ortega H, et al. Descriptions of spinal MRI lesions and definition of a positive MRI of the spine in axial spondyloarthritis: a consensual approach by the ASAS/OMERACT MRI study group. Ann Rheum Dis. 2012 Aug 1;71(8):1278–88.
46. Rodríguez-Fonseca OD, Aguiar P, García FMG, Llana BF, Díaz CV, Grande MLD, et al. 18F-FDG positron emission tomography as a marker of disease activity and treatment response in ankylosing spondylitis and psoriatic arthritis. Sci Rep. 2024 Aug 28;14:19907.
47. Wendling D, Blagosklonov O, Streit G, Lehuede G, Toussirot E, Cardot JC. FDG-PET/CT scan of inflammatory spondylodiscitis lesions in ankylosing spondylitis, and short term evolution during anti-tumour necrosis factor treatment. Ann Rheum Dis. 2005 Nov;64(11):1663–5.
48. Beckers C, Ribbens C, André B, Marcelis S, Kaye O, Mathy L, et al. Assessment of Disease Activity in Rheumatoid Arthritis with 18F-FDG PET. J Nucl Med. 2004 Jun 1;45(6):956–64.
49. Chaudhari AJ, Ferrero A, Godinez F, Yang K, Shelton DK, Hunter JC, et al. High-resolution 18F-FDG PET/CT for assessing disease activity in rheumatoid and psoriatic arthritis: findings of a prospective pilot study. Br J Radiol. 2016;89(1063):20160138.
50. Palmer WE, Rosenthal DI, Schoenberg OI, Fischman AJ, Simon LS, Rubin RH, et al. Quantification of inflammation in the wrist with gadolinium-enhanced MR imaging and PET with 2-[F-18]-fluoro-2-deoxy-D-glucose. Radiology. 1995 Sep;196(3):647–55.
51. Miese F, Scherer A, Ostendorf B, Heinzel A, Lanzman RS, Kröpil P, et al. Hybrid 18F-FDG PET–MRI of the hand in rheumatoid arthritis: initial results. Clin Rheumatol. 2011 Sep 1;30(9):1247–50.
52. de Groot M, Patel N, Manavaki R, Janiczek RL, Bergstrom M, Östör A, et al. Quantifying disease activity in rheumatoid arthritis with the TSPO PET ligand 18F-GE-180 and comparison with 18F-FDG and DCE-MRI. EJNMMI Res. 2019 Dec 19;9(1):113.
53. Khan IA, Vaccaro AR, Zlotolow DA. Management of Vertebral Diskitis and Osteomyelitis. Orthopedics. 1999 Aug;22(8):758–65.
54. Forrester DM. Infectious spondylitis. Semin Ultrasound CT MRI. 2004 Dec;25(6):461–73.
55. Stumpe KDM, Zanetti M, Weishaupt D, Hodler J, Boos N, von Schulthess GK. FDG Positron Emission Tomography for Differentiation of Degenerative and Infectious Endplate Abnormalities in the Lumbar Spine Detected on MR Imaging. Am J Roentgenol. 2002 Nov;179(5):1151–7.
56. Fahnert J, Purz S, Jarvers JS, Heyde CE, Barthel H, Stumpp P, et al. Use of Simultaneous 18F-FDG PET/MRI for the Detection of Spondylodiskitis. J Nucl Med. 2016 Sep 1;57(9):1396–401.
57. Fuster D, Tomás X, Mayoral M, Soriano A, Manchón F, Cardenal C, et al. Prospective comparison of whole-body 18F-FDG PET/CT and MRI of the spine in the diagnosis of haematogenous spondylodiscitis. Eur J Nucl Med Mol Imaging. 2015 Feb 1;42(2):264–71.
58. Altini C, Lavelli V, Niccoli-Asabella A, Sardaro A, Branca A, Santo G, et al. Comparison of the Diagnostic Value of MRI and Whole Body 18F-FDG PET/CT in Diagnosis of Spondylodiscitis. J Clin Med. 2020 May 22;9(5):1581.
59. Paez D, Sathekge MM, Douis H, Giammarile F, Fatima S, Dhal A, et al. Comparison of MRI, [18F]FDG PET/CT, and 99mTc-UBI 29-41 scintigraphy for postoperative spondylodiscitis—a prospective multicenter study. Eur J Nucl Med Mol Imaging. 2021;48(6):1864–75.
60. Demirev A, Weijers R, Geurts J, Mottaghy F, Walenkamp G, Brans B. Comparison of [18 F]FDG PET/CT and MRI in the diagnosis of active osteomyelitis. Skeletal Radiol. 2014 May;43(5):665–72.
61. Besson FL, Fernandez B, Faure S, Mercier O, Seferian A, Mignard X, et al. 18F-FDG PET and DCE kinetic modeling and their correlations in primary NSCLC: first voxel-wise correlative analysis of human simultaneous [18F]FDG PET-MRI data. EJNMMI Res. 2020 Jul 30;10(1):88.
62. Brendle CB, Schmidt H, Fleischer S, Braeuning UH, Pfannenberg CA, Schwenzer NF. Simultaneously acquired MR/PET images compared with sequential MR/PET and PET/CT: alignment quality. Radiology. 2013 Jul;268(1):190–9.

63. Boellaard R, Krak NC, Hoekstra OS, Lammertsma AA. Effects of noise, image resolution, and ROI definition on the accuracy of standard uptake values: a simulation study. J Nucl Med Off Publ Soc Nucl Med. 2004 Sep;45(9):1519–27.